Monthly Notices of the ROYAL ASTRONOMICAL SOCIETY

MNRAS **491,** 972–992 (2020)
Advance Access publication 2019 October 22

doi:10.1093/mnras/stz2952

3D hydrodynamic simulations of C ingestion into a convective O shell

R. Andrassy,[1,2,3]★ F. Herwig ,[1,2] P. Woodward[2,4] and C. Ritter[1,2]

[1]*Department of Physics & Astronomy, University of Victoria, PO Box 1700 STN CSC, Victoria, BC V8W 2Y2, Canada*
[2]*Joint Institute for Nuclear Astrophysics, Center for the Evolution of the Elements, Michigan State University, 640 South Shaw Lane, East Lansing, MI 48824, USA*
[3]*Heidelberg Institute for Theoretical Studies, Schloss-Wolfsbrunnenweg 35, D-69118 Heidelberg, Germany*
[4]*LCSE and Department of Astronomy, University of Minnesota, Minneapolis, MN 55455, USA*

Accepted 2019 October 13. Received 2019 October 4; in original form 2018 August 12

ABSTRACT

Interactions between convective shells in evolved massive stars have been linked to supernova impostors, to the production of the odd-Z elements Cl, K, and Sc, and they might also help generate the large-scale asphericities that are known to facilitate shock revival in supernova explosion models. We investigate the process of ingestion of C-shell material into a convective O-burning shell, including the hydrodynamic feedback from the nuclear burning of the ingested material. Our 3D hydrodynamic simulations span almost 3 dex in the total luminosity $L_{\rm tot}$. All but one of the simulations reach a quasi-stationary state with the entrainment rate and convective velocity proportional to $L_{\rm tot}$ and $L_{\rm tot}^{1/3}$, respectively. Carbon burning provides 14–33 per cent of the total luminosity, depending on the set of reactions considered. Equivalent simulations done on 768^3 and 1152^3 grids are in excellent quantitative agreement. The flow is dominated by a few large-scale convective cells. An instability leading to large-scale oscillations with Mach numbers in excess of 0.2 develops in an experimental run with the energy yield from C burning increased by a factor of 10. This run represents most closely the conditions expected in a violent O–C shell merger, which is a potential production site for odd-Z elements such as K and Sc and which may seed asymmetries in the supernova progenitor. 1D simulations may underestimate the energy generation from the burning of ingested material by as much as a factor 2 owing to their missing the effect of clumpiness of entrained material on the nuclear reaction rate.

Key words: convection – hydrodynamics – turbulence – stars: evolution – stars: interiors – stars: massive.

1 INTRODUCTION

Stellar evolution models show that evolved massive stars contain complex structures of nuclear burning shells deep in their cores, where most of the nuclear and binding energy is concentrated (e.g. Woosley, Heger & Weaver 2002; Davis, Jones & Herwig 2018). Energetic nuclear burning of different nuclear fuels (the most important being C, Ne, O, Si) often drives convective shells. The convective flows may entrain fresh fuel from layers above the shell, which burns and invigorates the convection. Under certain conditions, this positive feedback may result in a fuel ingestion runaway so rapid and violent that standard assumptions of 1D stellar evolution theory break down (Herwig et al. 2014).

Smith & Arnett (2014) suggest that hydrodynamic instabilities in evolved massive stars could be responsible for the eruptive mass-loss events preceding Type IIn supernovae (SN impostors, see also Smith et al. 2011b; Ofek et al. 2014; Arcavi et al. 2017), which comprise 6–12 per cent of all core collapse supernovae (Smith et al. 2011a). Such an instability, if it occurs deep in the core and shortly before the ultimate core collapse, could also provide the large-scale and large-amplitude seed perturbations that facilitate shock revival in multidimensional supernova explosion models (Couch & Ott 2013, 2015; Müller & Janka 2015; Müller et al. 2017). The instability would likely involve chemical mixing between nuclear burning shells in the core with some impact on element production in the star.

Ritter et al. (2018a), inspired by a merger of convective C- and O-burning shells in their stellar evolution model of a 15 $M_\odot$ star, investigate the unusual nucleosynthesis that occurs when a large amount of C-shell material is rapidly brought into the hot O-shell environment. They conclude, in agreement with earlier reports by Rauscher et al. (2002) and Tur, Heger & Austin (2007), that the odd-Z elements P, Cl, K, and Sc, which are underproduced in current galactic chemical evolution models, can be synthesized this way. Similarly, Clarkson, Herwig & Pignatari (2018) find a highly energetic H–He convective shell interaction event in their model of a 45 $M_\odot$ Pop III star when the gap between convective H and He shells

★ E-mail: robert.andrassy@h-its.org

closes. Their single-zone calculations of the resulting i-process nucleosynthesis can reproduce certain intermediate-mass-element features in the abundance distribution of the most Fe-poor CEMP-no (C-enhanced metal-poor) stars observed to date. However, all of these implications for stellar nucleosynthesis should be considered qualitative, because they depend on rather uncertain 1D models of rapidly evolving convective-reactive flows, which are inherently 3D.

2D simulations of the violent shell burning that occurs in supernova progenitors shortly before core collapse had become feasible in the 1990s as demonstrated by Arnett (1994). Bazan & Arnett (1994), Bazan & Arnett (1998), and Arnett & Meakin (2011) further improved the methodology and ultimately included in their (still 2D) simulations everything from the upper parts of the Si core to the H envelope. They reported on convection dominated by large-scale structures, significant deviations from spherical symmetry as well as hotspot burning of convectively entrained ^{12}C just minutes before core collapse. More recently, 3D simulations have been constructed (Meakin & Arnett 2007a; Couch & Ott 2015; Jones et al. 2017; Müller et al. 2017; Mocák et al. 2018), showing that 2D simulations significantly overestimate the amplitude of convective motions (Meakin & Arnett 2006).

Jones et al. (2017, J17 hereafter) presented a set of idealized 3D hydrodynamic simulations constructed to closely resemble a convective O-burning shell in their 1D model of a 25 $M_\odot$ star. They derive a mass entrainment rate at the upper convective boundary of $5.4 \times 10^{-7}\,M_\odot\,s^{-1}$ for the luminosity of the 1D model. It would only take ∼6 d – less than the lifetime of the O shell – for the O-shell convection to reach the bottom of a neighbouring convective C-burning shell at this rate. Some material from the C shell could thus be entrained into the hot O-shell environment or the two shells might even merge, as suggested by the nuclear astrophysics results of Ritter et al. (2018a). As a first essential step towards a full merger simulation, we construct a set of 3D hydrodynamic simulations to investigate the dynamics of C entrainment from a stable layer into a convective O-burning shell. We intend to answer questions like: How strong is the feedback from C burning on the flow in the shell? How does it depend on the O-luminosity of the shell? Is the entrainment process stable? Does it ever lead to a fuel ingestion runaway such as that described by Herwig et al. (2014)? How is the luminosity–entrainment rate relation measured by J17 affected by C burning?

2 METHODS

2.1 1D stellar-evolution model

The 3D simulations described in this work are based on the 1D evolution model of a 25 $M_\odot$ star computed by J17 using the MESA code (Paxton et al. 2011, 2013, 2015). The stellar model's initial metallicity is $Z = 0.02$. Rotation is not considered and the Schwarzschild criterion is used to delineate convective regions. Mixing of chemical species at convective boundaries is modelled using a diffusion coefficient decaying exponentially with an e-folding length $\frac{1}{2} f_{\rm CBM} H_p$, where $f_{\rm CBM} = 0.022$ is used for all convective boundaries before core C ignition except the bottom boundaries of burning shells where $f_{\rm CBM} = 0.005$ is set and $f_{\rm CBM} = 0.002$ is used for all convective boundaries after core C ignition.

We focus on the first shell O-burning phase that spans approximately from 21 to 4 d before core collapse (Fig. 1). With the start of shell O burning, a convection zone appears and grows in size until its mass reaches 0.66 $M_\odot$. The outward propagation of the upper convective boundary slows down at this point and further growth is limited to an additional 0.08 $M_\odot$ over 7 d, after which convection recedes. At the point of the shell's maximum extent there is 0.18 $M_\odot$ of stable material separating the O shell from the C shell and there is no mixing between the two in the stellar evolution model.

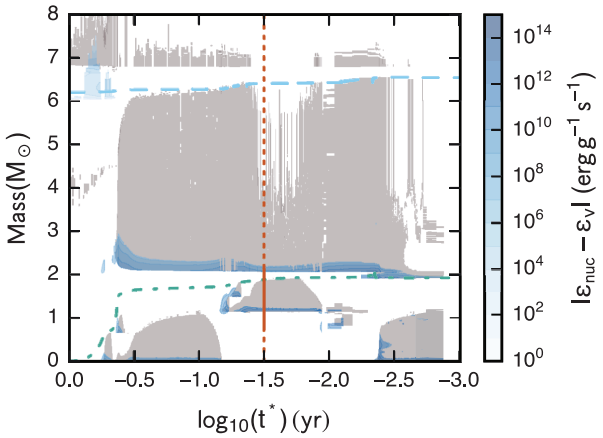

Figure 1. Kippenhahn diagram showing the core structure of the 25 $M_\odot$MESA model as a function of time until core collapse. Shades of blue show the energy generation rate and grey regions are convective. The light-blue dashed and turquoise dot–dashed lines are the boundaries of the He- and C-free cores, respectively. The red vertical line indicates the model that was used to construct the initial condition of the 3D simulations. The solid portion of that line marks the radial extent of the 3D model.

2.2 3D `ppmstar` simulations

2.2.1 `ppmstar` *code*

We use the PPMSTAR code of Woodward, Herwig & Lin (2015). It is an explicit Cartesian-grid-based code for 3D hydrodynamics built around the Piecewise-Parabolic Method (PPM; Woodward & Colella 1981, 1984; Colella & Woodward 1984; Woodward 1986, 2007). The code advects the fractional volume FV of the lighter fluid in a two-fluid scheme using the Piecewise-Parabolic Boltzmann method (PPB; Woodward 1986; Woodward et al. 2015). In 1D, PPB is formally fifth-order accurate, and in our 3D flows, despite our use of directional splitting, it delivers greatly improved accuracy over PPM advection. The benefits of PPB advection can be seen in the 2D code comparison in Joggerst et al. (2014) and in the 3D code comparison on a Rayleigh–Taylor problem in Ramaprabhu et al. (2012). PPB achieves its greater accuracy in part by updating 10 lower order moments of the distribution of FV within each cell. With this additional information to work with, it should not be surprising that we usually find its results to be as good or better than PPM advection run on a grid with twice the number of grid cells in each dimension. Also, this additional, subcell information updated by PPB allows us to describe sharp transitions on the grid from a state with no tracked fluid, FV = 0, to only tracked fluid, FV = 1, without resorting to the discontinuity detection and steepening methods of PPM advection. The result is that thin transitions can be advected with minimal diffusion and also without the changes in the algorithmic description that can give rise to small glitches with PPM advection that can be subsequently amplified at physically unstable interfaces. This feature can be observed in the 3D test problem motivated by inertial confinement fusion that is discussed in Woodward et al. (2012). We also note that our stellar convection flows involve Mach numbers of the order of 10^{-2}. It is therefore

especially important that the PPM scheme involves interpolated estimates of the values of variables at cell edges that are derived from cubic polynomials. This feature makes PPM well behaved when the scheme is applied at low Mach numbers, and hence low flow Courant numbers, when these edge values play an especially important role.

The time-step is fixed and corresponds to CFL = 0.75 at $t = 0$. We impose constraints where FV approaches the special values of zero and unity. We do not constrain nuclear burning rates with the exception of not burning more mass than is available in the computation cell and not burning trivial amounts of material. The reader is referred to Woodward (2007) and Woodward et al. (2015) for further details of the overall scheme and of the approximate Riemann solver implemented in PPMSTAR. The code was designed with strong emphasis on parallel efficiency and it has performed past simulations of shell convection on up to 440 000 CPU cores on the NCSA Blue Waters computer (Herwig et al. 2014; Woodward et al. 2015; Woodward, Herwig & Wetherbee 2018).

The version of PPMSTAR used in this work has four data output channels, all of which we use in this work:

(i) Full-resolution 3D data cubes. Variable-dependent non-linear transforms are applied to compress the data to a single byte per voxel, which is sufficient for flow visualization purposes. The fractional volume variable is saved at twice the original grid resolution to make use of the PPB subcell information.

(ii) 3D data cubes downsampled by averaging blocks of 4^3 grid cells, which decreases spatial resolution by a factor of 4 and the amount of data by a factor of $4^3 = 64$. Variable-dependent non-linear transforms are applied to further compress the data to 2 bytes per voxel, which is sufficient for both flow visualization and data analysis.

(iii) Spherical averages measured in 80 radial, space-filling tetrahedra, which we call *buckets* (see fig. 17 of J17 for their exact distribution). The buckets are ideal for rapid analysis of time series whenever angular resolution is not critical.

(iv) Spherical averages over the full solid angle, which we use to study global properties of the flow, mass transport, or burning rates.

All of this output is computed on-the-fly and written to disc at regular time intervals without ever interrupting the hydrodynamic simulation.

2.2.2 3D simulation setup

The initial stratification of our simulations is the same as the one used by J17 and is composed of three polytropes that approximate the stratification of the MESA model. The bottom and top polytropes are stable against convection and the middle one is adiabatic. The polytropic stratification is close to that of the MESA model throughout the volume included in the 3D simulation, see fig. 4 of J17, and little could be gained by modelling the stratification in more detail given the differences in the equation of state described below. The polytropic model is also resolved on the 3D computational grid by construction, which is not true about the MESA model. The stratification changes significantly on the simulation time-scale when we drive the convection strongly (see Section 3.3), but the change is negligible when the driving luminosity is close to that of the MESA model. The C shell and outer layers of the star as well as the inner core are not included. We impose boundary conditions at radii of 3.5 and 9.2 Mm such that the flow remains confined between the two spherical walls and material fluxes through them vanish. The boundaries are rough on small scales because of the Cartesian geometry of the computational grid. This effect is not expected to influence our results, because we restrict the time interval of our analysis such that the convective boundary does not get too close to the outer boundary condition.[1]

We use the equation of state of an ideal monatomic gas in our simulations. This is a surprisingly good approximation owing to the high temperature typical of O-shell convection. Despite high density, degeneracy pressure is limited to 3–6 per cent of the total pressure in the shell. Its contribution increases to ~ 20 per cent in the stable layer below the shell, which we only use as a buffer zone that forces the convective flows to turn around. Our two-fluid models (see below) also cannot include the composition step at the bottom of the shell, so we refrain from any attempts to quantify mixing at the shell's lower boundary in this work. Radiation pressure does not exceed 25 per cent of the total pressure in the shell. A new version of the PPMSTAR code, which includes radiation pressure, is already being tested and we intend to quantify the influence of radiation pressure on stellar convection in a future publication. The initial stratification of the PPMSTAR runs is compared with that of the MESA model in fig. 4 of J17.

The upper stable layer is initially filled with fluid $\mathcal{F}_\mathrm{C}$ and the rest is fluid $\mathcal{F}_\mathrm{O}$. There is a 0.25 Mm thick smooth transition in the fractional volume FV of fluid $\mathcal{F}_\mathrm{C}$ centred at the radius of 8.08 Mm such that FV = 0 below the transition layer and FV = 1 above it (see fig. 20 of J17). Each of the two fluids corresponds to a mixture of chemical elements. The individual abundances of these elements are not evolved in time and only those that enter our simplified reaction network (see Section 2.2.4) need to be known. The concentration of ^{16}O in fluid $\mathcal{F}_\mathrm{O}$, $X_{16} = 0.382$, is taken from the MESA model directly. The stable layer above the O shell (fluid $\mathcal{F}_\mathrm{C}$) is for the purposes of our experiment assumed to be rich in ^{12}C with the mass fraction $X_{12} = 0.13$. This concentration is five times larger than that in the C shell of the MESA model. We do this to speed up the simulations' transition to a quasi-stationary state. Despite this increase in X_{12}, we use the same mean molecular weights as J17 ($\mu_1 = 1.802$ for $\mathcal{F}_\mathrm{C}$ and $\mu_2 = 1.848$ for $\mathcal{F}_\mathrm{O}$) to allow direct comparison of entrainment rates. The radial profile of the squared Brunt–Väisälä frequency N^2 in this transition layer closely resembles that of the MESA model, see fig. 6 of J17.

J17 used a volume heating term to drive convection. We have implemented an O-burning prescription in the code (see Section 2.2.4) and introduced a parameter (f_OO in Table 1) to scale the heat output and reach different driving luminosities without having to change the initial stratification. Fig. 2 shows that the heating rate distribution is more concentrated to the bottom of the shell in our simulations than in those of J17. Neutrino cooling balances all of the shell's luminosity in the MESA model. We do not consider this effect and estimate its influence on the mass entrainment rate at the end of Section 3.2. However, our O-burning prescription with $f_\mathrm{OO} = 1$ (run I2, see Table 1) provides a driving luminosity $L_\mathrm{OO} = 4.27 \times 10^{10}\,\mathrm{L}_\odot$, which is comparable to the maximum luminosity $L = 5.2 \times 10^{10}\,\mathrm{L}_\odot$ reached in the O shell of the MESA model when both nuclear heating and neutrino cooling are considered.

2.2.3 Simulations

Simulations presented in this work are listed in Table 1 along with some of their global properties. We investigate the luminosity

[1] Run I11 is an exception, see Section 3.6.

Table 1. Properties of the 3D PPMSTAR simulations presented in this work. The first three columns give the run identification code, grid resolution, and the total length of the simulation. If C burning is included the 'nuc. net.' column gives which nuclear network was used. Energy output from nuclear reactions is scaled by factors $f_{\rm OO}$ (^{16}O + ^{16}O), $f_{\rm CC}$ (^{12}C + ^{12}C), and $f_{\rm CO}$ (^{12}C + ^{16}O) and the resulting contributions to the total luminosity $L_{\rm tot}$ are $L_{\rm OO}$, $L_{\rm CC}$, and $L_{\rm CO}$. The last four columns give the entrainment rate $\dot{M}_{\rm e}$, rms convective velocity $v_{\rm rms}$, overturning time-scale $\tau_{\rm conv}$, and a mass-weighted Mach number in the convection zone. The values of $L_{\rm OO}$, $L_{\rm CC}$, $L_{\rm CO}$, $L_{\rm tot}$, $\dot{M}_{\rm e}$, $v_{\rm rms}$, $\tau_{\rm conv}$, and Ma correspond to averages over a time window several convective overturns long, which was the same for all variables but varied from run to run. All runs of the D series except for D23 were already presented by J17.

Id	Grid	$t_{\rm sim}$ (min)	nuc. net.	$f_{\rm OO}$	$f_{\rm CC}$	$f_{\rm CO}$	$L_{\rm OO}$ ($L_\odot$)	$L_{\rm CC}$ ($L_\odot$)	$L_{\rm CO}$ ($L_\odot$)	$L_{\rm tot}$ ($L_\odot$)	$\dot{M}_{\rm e}$ ($M_\odot$ s^{-1})	$v_{\rm rms}$ (km s^{-1})	$\tau_{\rm conv}$ (min)	Ma
D1	768^3	55.2	–	–	–	–	–	–	–	1.18 (11)	1.15 (−6)	38.0	3.46	9.40 (−3)
D2	1536^3	27.3	–	–	–	–	–	–	–	1.18 (11)	1.33 (−6)	39.1	3.37	9.70 (−3)
D5	768^3	37.2	–	–	–	–	–	–	–	5.91 (11)	8.07 (−6)	66.7	2.05	1.65 (−2)
D6	768^3	41.3	–	–	–	–	–	–	–	1.18 (12)	1.68 (−5)	85.8	1.65	2.13 (−2)
D8	768^3	36.2	–	–	–	–	–	–	–	2.95 (11)	3.60 (−6)	52.2	2.58	1.29 (−2)
D9	768^3	43.5	–	–	–	–	–	–	–	2.95 (12)	3.83 (−5)	118	1.27	2.92 (−2)
D10	768^3	43.7	–	–	–	–	–	–	–	5.91 (12)	7.94 (−5)	149	1.03	3.71 (−2)
D23	768^3	53.4	–	–	–	–	–	–	–	2.95 (10)	9.50 (−8)	21.0	6.14	5.17 (−3)
I2	768^3	242	NET 1	1	1	–	4.27 (10)	8.30 (9)	–	5.10 (10)	3.14 (−7)	27.9	4.74	6.85 (−3)
I4	768^3	76.3	NET 1	2.7	1	–	1.16 (11)	2.84 (10)	–	1.45 (11)	1.09 (−6)	40.3	3.34	9.89 (−3)
I5	768^3	39.5	NET 1	13.5	1	–	5.79 (11)	2.54 (11)	–	8.33 (11)	9.66 (−6)	117	1.94	1.78 (−2)
I11	768^3	13.5	NET 1	13.5	10	–	8.05 (11)	1.32 (13)	–	1.40 (13)	2.24 (−4)	181	0.82	4.46 (−2)
I12	768^3	46.9	NET 1	2.7	–	–	1.16 (11)	–	–	1.16 (11)	7.53 (−7)	35.3	3.73	8.67 (−3)
I13	768^3	23.1	NET 1	67.5	1	–	5.10 (12)	2.54 (12)	–	7.63 (12)	1.07 (−4)	147	1.02	3.63 (−2)
I14	1152^3	22.4	NET 1	67.5	1	–	6.26 (12)	2.87 (12)	–	9.13 (12)	1.18 (−4)	163	0.95	4.01 (−2)
I15	1152^3	58.3	NET 1	2.7	1	–	1.16 (11)	3.37 (10)	–	1.50 (11)	1.37 (−6)	41.6	3.23	1.03 (−2)
I16	768^3	73.8	NET 2	2.7	1	1	1.16 (11)	2.25 (9)	2.10 (10)	1.39 (11)	9.73 (−7)	39.3	3.41	9.66 (−3)
I17	768^3	27.8	NET 2	67.5	1	1	4.49 (12)	3.97 (11)	3.59 (11)	5.25 (12)	6.30 (−5)	139	1.06	3.44 (−2)

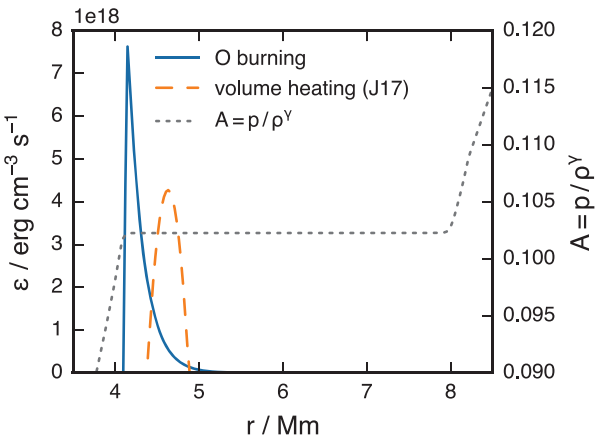

Figure 2. Comparison of the distribution of the heating rate per unit volume as given by the O-burning prescription used in this work with that given by the volume heating prescription of J17. Both distributions are normalized to give the same luminosity of 10^{11} $L_\odot$. The flat part of the entropy profile $A = p/\rho^\gamma$ is the convection zone.

dependence of C ingestion in the series of runs I2 (O-luminosity enhancement factor $f_{\rm OO} = 1$), I4 ($f_{\rm OO} = 2.7$), I5 ($f_{\rm OO} = 13.5$), and I13 ($f_{\rm OO} = 67.5$) done on a 768^3 grid (see Table 1). C burning was only turned on at $t = 74$ min in run I2 by mistake. Runs I14 and I15 are higher resolution versions of runs I13 and I4, respectively, done on a 1152^3 grid to estimate any resolution dependence. We experimentally turned C burning off in run I12 and enhanced the energy release from C burning by the factor $f_{\rm CC} = 10$ in run I11, which are otherwise like runs I4 and I5, respectively. All the runs mentioned so far use the same C-burning reaction network NET 1 (see the next section). We investigate how our results depend on the assumptions about C-burning reactions using runs I16 and I17, which are like runs I4 and I13, respectively, but they use an alternative reaction network NET 2. We also use for the analysis runs D1, D2, D5, D6, D8, D9, and D10 of J17, in which convection is driven by a volume heating term and the burning of the entrained material is not considered. Finally, we have added run D23 to extend the D-series of runs towards even lower luminosities.

2.2.4 *Reaction network*

Convection in the shell is driven by O burning, which we compute using equation (18.75) of Kippenhahn, Weigert & Weiss (2012), neglecting electron screening. We do not model the slow change in the O mass fraction due to this burning process. The temperature is slightly overestimated in the shell because of our neglect of radiation pressure in the equation of state. We correct the temperature profile before computing energy generation rates using the transformation

$$\vartheta = 1.022\, T_9^{0.64}, \tag{1}$$

where T_9 is the temperature in units of 10^9 K and the numerical coefficients were adjusted until a close fit to the temperature profile of the MESA model was obtained. In order to model the drop in T_9 and X_{16} at the bottom of the O shell seen in the MESA model, we further modify the temperature profile using either the transformation

$$\Theta = \frac{1}{2}\{1 - \tanh[200(\vartheta - 2.24)]\}\,\vartheta, \tag{2}$$

or the transformation

$$\Theta = \frac{1}{2}\{1.01 - 0.99\tanh[0.07(\rho_3 - 1845)]\}\,\vartheta, \tag{3}$$

where ρ_3 is the density in units of 10^3 g cm^{-3}. Equation (2) is used in low- and medium-luminosity runs I2, I4, I5, I12, I15, and I16, but the shallowness of the temperature profile in the lower stable layer makes Θ too sensitive to the relatively large changes in the stratification we see in high-luminosity runs. Equation (3) is much

less sensitive to such changes.[2] We use it in runs I11, I13, I14, and I17.

There would be a large number of nuclear reactions involved in the burning of the ingested material in an actual star. However, the purpose of this study is not to replicate in detail a shell interaction found in a particular stellar evolution model. Instead, we aim to study the general behaviour of the ingestion process when the burning of the ingested material feeds back on to the convective flow. We use two simple reaction networks based on our earlier 1D calculations with a large network (Ritter et al. 2018a):

(i) NET 1: $^{12}C(^{12}C,\alpha)^{20}Ne$ followed by $^{16}O(\alpha,\gamma)^{20}Ne$. The rate of the former reaction is computed from the rate of $^{12}C + {}^{12}C$ given by Caughlan & Fowler (1988) with the neutron and proton branches subtracted according to the branching ratios used by Dayras, Switkowski & Woosley (1977) and Pignatari et al. (2013). The α particle is assumed to be immediately captured in the latter reaction. The Q values of the two reactions, 4.62 and 4.73 MeV, respectively, are summed.

(ii) NET 2: All channels (n, p, γ) of $^{12}C + {}^{12}C$ and $^{12}C + {}^{16}O$. The rates are taken from Caughlan & Fowler (1988) and the Q values are 3.19 and 5.26 MeV, respectively. The subsequent reactions induced by the released neutrons and protons are not considered for simplicity as many temperature-dependent reaction paths are possible.

The rate of the $^{12}C + {}^{12}C$ reaction scales with the square X_{12}^2 of the concentration of ^{12}C and it is thus important when the concentration is high (i.e. when the entrainment rate is high). On the other hand, the $^{12}C + {}^{16}O$ reaction becomes important at low concentrations (i.e. low entrainment rates) owing to the reaction's being linear in X_{12}. Having two reaction networks allows the reader to judge how different the outcome is when the entrained material only reacts with itself (NET 1) compared to a situation in which reactions with the other fluid are also possible (NET 2). Additionally, we used the PPN (Pignatari et al. 2016; Ritter et al. 2018b) code to confirm that our neglect of electron screening is justified, because it is a 10–20 per cent effect for the range of densities and temperatures relevant to the O-shell problem.

Our implementation of nuclear burning in the two-fluid approximation is as follows. The fractional volumes FV of fluid $\mathcal{F}_C$ and $1 -$ FV of fluid $\mathcal{F}_O$ are first converted into molar fractions Y_C and Y_O of the ^{12}C and ^{16}O reactants, taking into account that only the fractions $f_C = 0.187$ and $f_O = 0.540$ of all nuclei in each of the two fluids represent the reactants.[3] This reflects our mental picture that each of the fluids has some internal composition, which is not evolved. A change dY_C in the molar fraction Y_C of ^{12}C is then computed using the equations of nuclear burning (see e.g. Chapter 18 of Kippenhahn et al. 2012) with the rates described above. Whenever a molar fraction dY_C of ^{12}C nuclei needs to be removed from fluid $\mathcal{F}_C$, we are forced to remove the molar fraction dY_C/f_C of fluid $\mathcal{F}_C$, because the internal composition of this fluid cannot change in our two-fluid model. The burning process also cannot change the total density of the two-fluid mixture, so the amount of fluid $\mathcal{F}_C$ burnt is replaced by an equivalent amount of fluid $\mathcal{F}_O$. While this qualitatively captures the increase in the mean molecular weight μ upon nuclear fusion, we would need to introduce more fluids into the model to make the change in μ quantitatively correct. The heat released from the nuclear reactions is added after every 1D pass to maximize the temporal accuracy of the numerical scheme.

[2]Equation (3) also makes sure that Θ never drops to zero, which would cause numerical problems in the energy generation module if a negligible but non-zero amount of the C-rich fluid got below the convection zone and the energy generation rate calculation was executed. This sometimes happens when convection becomes too vigorous.

[3]We make use of the fact that the fractional volume of fluid $\mathcal{F}_C$ entrained into the O shell is small, so we only need to consider ^{16}O nuclei present in the dominant fluid $\mathcal{F}_O$.

3 RESULTS

3.1 C entrainment and burning

The flow field in our simulations is dominated by a few large-scale convection cells (Fig. 3). They cause shear flows as they turn over at the upper convective boundary, but, as Woodward et al. (2015) and J17 describe in detail, entrainment does not occur where the shear is the strongest. It rather occurs at places where two neighbouring flows sliding along the boundary collide and are forced back into the convection zone by the global flow topology, dragging slivers of fluid $\mathcal{F}_C$ along.

According to our assumption, the concentration of ^{12}C in fluid $\mathcal{F}_C$ is five times higher than that in the stellar evolution model (see Section 2.2.2), so we can see some energy generation due to $^{12}C + {}^{12}C$ reactions in the upper stable layer in Fig. 3, but the burning is not strong enough to establish a new convection zone on the time-scales considered. $^{12}C + {}^{16}O$ reactions do not contribute in the stable layer, because we only compute reactions involving ^{12}C from fluid $\mathcal{F}_C$ and ^{16}O from fluid $\mathcal{F}_O$ and there is no fluid $\mathcal{F}_O$ in the upper stable layer. The concentration of $\mathcal{F}_C$ drops by orders of magnitude at the upper boundary as the mixing process reduces the buoyancy of the fluid mixture to make it possible for convection to pull it to the bottom of the convection zone. Therefore, C-burning reactions are virtually absent in the upper half of the convection zone and they are only rekindled at the bottom owing to an increase in temperature.

Because the $^{12}C + {}^{12}C$ reaction rate depends on the square of the concentration X_{12} of ^{12}C, the burning time-scale in runs with a significant contribution from the $^{12}C + {}^{12}C$ reaction becomes shorter when the driving luminosity and hence also the mass entrainment rate is increased. The burning time-scale is a few times longer than the convective overturning time-scale in the low-luminosity run I2 ($f_{OO} = 1$), which results in a rather flat fractional volume profile of the entrained C-rich fluid, see Fig. 4. On the other hand, there is a significant fractional volume gradient in the convection zone of the high-luminosity run I13 ($f_{OO} = 67.5$), in which the two time-scales are comparable. This gradient causes the C-burning layer to be more extended in run I13 than in run I2 (Fig. 4). The burning time-scale for the $^{12}C + {}^{16}O$ reaction is independent of X_{12}.

Fig. 3 also shows that there is a lot of large-scale structure in the distribution of the entrained material. We show in Section 3.5 that these inhomogeneities are the main cause of the asymmetric distribution of the burning rate (Fig. 3) with temperature fluctuations playing a secondary role. The asymmetry is the most pronounced at the upper end of the luminosity range considered.

All runs, with the exception of run I11, reach a quasi-stationary state in which there is a close balance between mass entrainment and burning and the concentration of fluid $\mathcal{F}_C$ in the convection zone stays approximately constant. Some selected properties of our simulations are summarized in Table 1. The following three sections present the detailed evolution of the simulations in terms of the entrainment rate, luminosity, and velocity field. We analyse 3D fluctuations of the most relevant quantities in Section 3.5 and, finally, we discuss the unstable run I11 in Section 3.6.

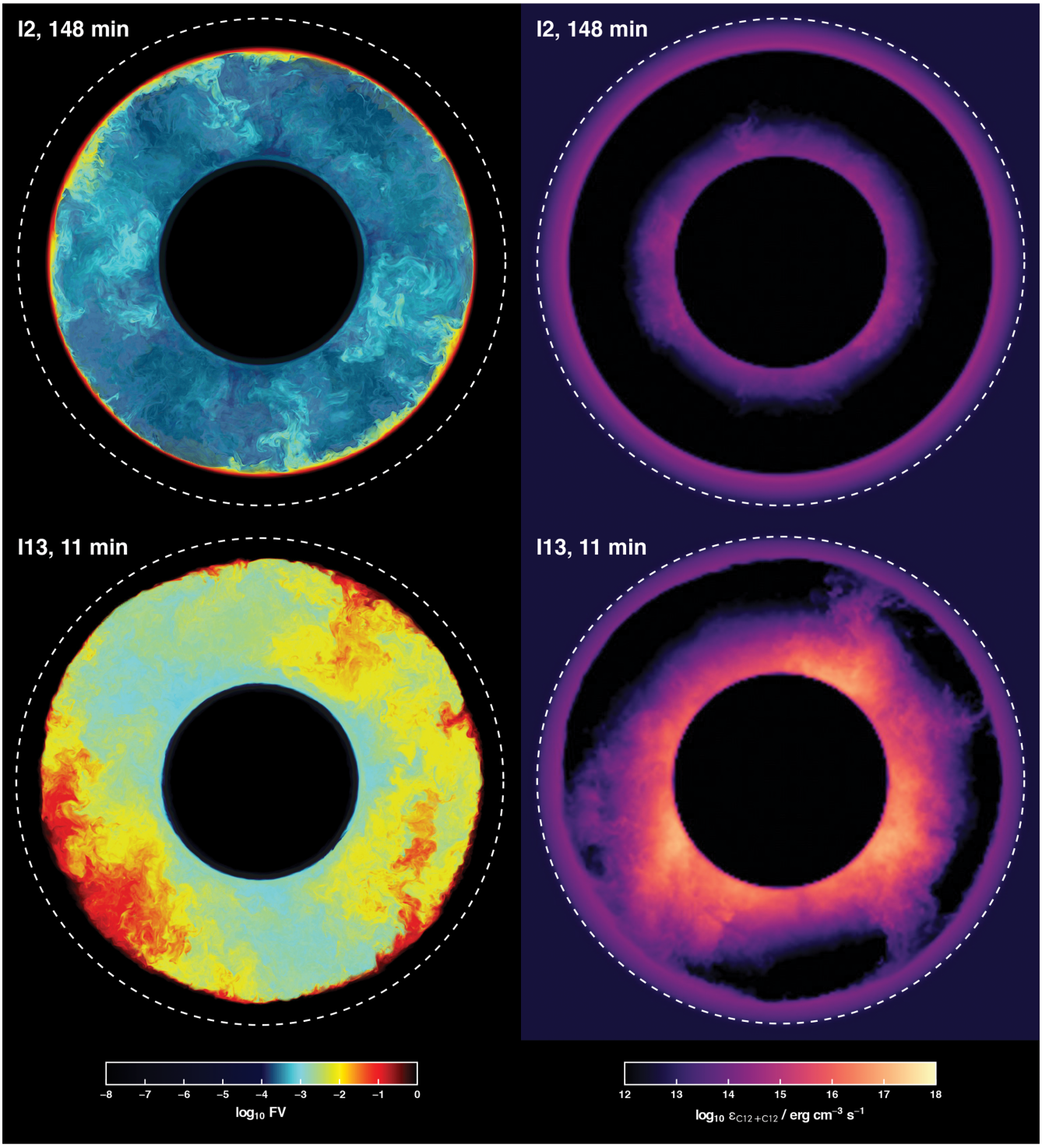

Figure 3. Renderings showing a thin slice through the computational box in terms of the fractional volume FV of fluid $\mathcal{F}_C$ (left-hand panels) and energy generation rate from the $^{12}C + {}^{12}C$ reaction (right-hand panels) in runs I2 ($f_{OO} = 1$) and I13 ($f_{OO} = 67.5$). The two runs differ by a factor of ∼170 in the total luminosity at the points in time corresponding to the renderings. The energy generation rates were computed by post-processing data downsampled from 768^3 to 192^3, in which all 3D fluctuations except those in FV were neglected, see Section 3.5. The white dashed circles correspond to the outer boundary condition.

3.2 Entrainment rate

The mass $M_e(t)$ of the C-rich fluid $\mathcal{F}_C$ entrained into the convection zone by time t is the sum

$$M_e(t) = M_p(t) + M_b(t) \tag{4}$$

of the mass $M_p(t)$ of $\mathcal{F}_C$ present in the convection zone at time t and the mass $M_b(t)$ of $\mathcal{F}_C$ burnt in the convection zone by time t.

To compute $M_p(t)$, we employ the method of J17. We first determine the radius $r_{ub}(t)$ of the upper boundary of the convection zone as defined by the position of the steepest decline in the spherically averaged rms tangential velocity $v_\perp$, and the radius

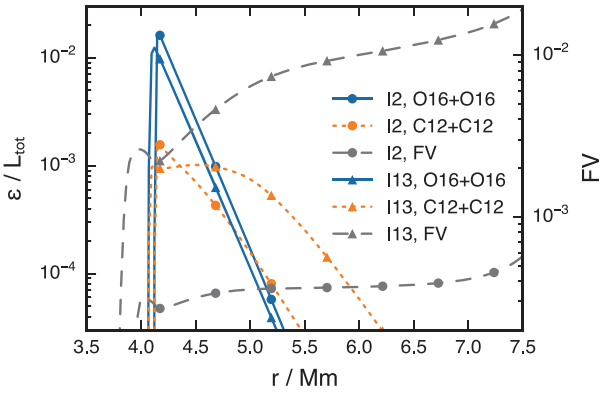

Figure 4. Comparison of the energy generation rates per unit volume in the low-luminosity run I2 ($f_{OO} = 1$) with those in the high-luminosity run I13 ($f_{OO} = 67.5$). The energy generation rate ε is normalized by the total luminosity L_{tot} and the radial profiles of the fractional volume FV of the entrained fluid are shown for comparison. The radial profiles correspond to 148 min in I2 and to 11 min in I13 with time averaging over two convective overturning time-scales applied around these points in time in both cases.

$r_{top}(t) = r_{ub}(t) - H_{v,\,ub}(t)$, where $H_{v,\,ub}(t) = v_\perp |\partial v_\perp / \partial r|^{-1}$ is the scale height of $v_\perp$ to be evaluated at $r_{ub}(t)$. $M_p(t)$ is then the volume integral of the density of fluid $\mathcal{F}_C$ inside the radius $r_{top}(t)$.[4]

The burnt mass $M_b(t)$ is given by a volume and time integral of the mass burning rate in the convection zone, which is computed from reaction rates in a way analogous to the luminosity computation described in Section 3.3. Since the burning is concentrated to the lower part of the convection zone, we simply integrate up to the radius of 7.5 Mm, which is slightly below the initial location of the upper boundary of the convection zone.

Fig. 5 shows the entrained mass $M_e(t)$ for runs I2 ($f_{OO} = 1$) and I13 ($f_{OO} = 67.5$), which are the least and most luminous of the 768^3 I-series runs with quasi-stationary C burning, respectively. In run I2, $M_p(t)$ steadily increases until C burning is turned on at $t = 74$ min (see Section 2.2.3), after which it takes 3–5 convective overturns to reach a quasi-stationary state with an entrainment rate of $\dot{M}_e = 3.14 \times 10^{-7}\,M_\odot\,s^{-1}$. $\dot{M}_e$ decreases again very late in the run, which is likely caused by the steepening of the entropy gradient at the upper convective boundary due to the energy release from C burning at the bottom of the upper stable layer (see Section 3.1). This effect is negligible in run I13 (Fig. 5), which is 12 × shorter than I2 but, owing to the strong driving of convection, it reaches an entrainment rate so high that all of the upper stable layer is ultimately entrained within the simulated time. The quasi-stationary entrainment rate is $\dot{M}_e = 1.07 \times 10^{-4}\,M_\odot\,s^{-1}$ in I13. In light of the linear dependence of the entrainment rate on the total luminosity discussed in the next paragraph, it is surprising that the entrainment rate is essentially constant while the total luminosity more than doubles between 5 and 14 min of simulation time, see Fig. 7. This might be due to the following opposing effect: as the convective boundary moves further into the stable layer, the entropy jump across the boundary increases, which hinders mass entrainment. The entrainment rate only starts to increase at $t \approx 14$ min when the convective boundary has reached the radius of 8.6 Mm (starting from 8.0 Mm at $t = 0$) and half of the upper stable layer (in terms of radius) has been engulfed by the convection. The scale height $H_{v,ub}$ of the velocity profile starts increasing at that point. We see the same effect in similarly luminous runs I14 ($f_{OO} = 67.5$, NET 1), I17 ($f_{OO} = 67.5$, NET 2), and also in run D10 that does not include C burning, although it only occurs when the boundary has reached 8.75 Mm in D10. A likely explanation is that the outer boundary condition at 9.2 Mm starts to influence the flows at the top of the convection zone when the upper stable layer has become too thin. The last 3 min of run I13 are not shown in Fig. 5, because velocity amplitudes in the upper stable layer become so large in that time interval that the velocity-gradient-based method of locating the convective boundary becomes unusable. We also exclude from the entrainment analysis the last few minutes of runs I14, I17, and D10 for the same reason.

The I-series runs with either C-burning network confirm the linear relation between the entrainment rate and the total luminosity established by the D-series runs of J17, see Fig. 6. Run I11 is close to the scaling relation despite its unstable nature (see Section 3.6 for details). That the entrainment rates in low-luminosity runs fall below the linear trend is likely caused by the limited length of our simulations. One would ideally want to run a simulation of convective boundary mixing at least until all of the initial transition layer between the two fluids has been entrained and a new boundary has been formed, consistent with the properties of the convective flows and of the entrainment process. However, this is very expensive to achieve even on a 768^3 grid when the luminosity is low. The initial transition layer at the upper boundary contains $2.7 \times 10^{-2}\,M_\odot$ of fluid $\mathcal{F}_C$, but only $3.3 \times 10^{-3}\,M_\odot$ was entrained in the low-luminosity run I2 ($5.1 \times 10^{10}\,L_\odot$, see Fig. 5), which involved 3.8×10^6 time-steps. The entrainment rate may depend on the assumed structure of the transition layer in such cases. On the other hand, most of the initial transition layer was entrained in runs D5 ($5.9 \times 10^{11}\,L_\odot$, see fig. A1 of J17) and I5 ($8.3 \times 10^{11}\,L_\odot$, see Fig. B1) and the layer was completely engulfed by convection in all runs with $L_{tot} \geq 10^{12}\,L_\odot$.

Some fraction of the entrainment rates reported here is a consequence of the gradual increase in the mean entropy of the convection zone, which results from our neglect of neutrino cooling. The rate of convective boundary migration due to this effect is proportional to the rate of change of entropy $A = p/\rho^\gamma$ in the convection zone and inversely proportional to the slope of $A(m)$ in the relevant part of the stable layer, where m is the enclosed mass coordinate. During the time interval in which we determined the entrainment rate $\dot{M}_e = 1.07 \times 10^{-4}\,M_\odot\,s^{-1}$ in run I13 (see Fig. 5), we measure $(\partial A/\partial t)_{conv} = 7.3 \times 10^{-6}\,s^{-1}$ in the convection zone.[5] The slope $(\partial A/\partial m)_{stab} = 1.4 \times 10^{-1}\,M_\odot^{-1}$ fits well the stable stratification above the convection zone at $t = 0$. As the entropy in the convection zone increases, stable material is rendered unstable at the rate $\dot{M}_A = (\partial A/\partial t)_{conv} / (\partial A/\partial m)_{stab} = 5.2 \times 10^{-5}\,M_\odot\,s^{-1}$, which accounts for 49 per cent of the entrainment rate in this run. This fraction should not depend on the driving luminosity L_{tot}, because both $(\partial A/\partial t)_{conv}$ and $\dot{M}_e$ scale in proportion to L_{tot}. The estimate just presented excludes the effect of neutrino cooling on convective velocity. Meakin & Arnett (2007b) include neutrino cooling in their 3D simulation of a similar O shell and the radial velocity in their simulation is indeed lower than what our scaling law predicts (see

[4]The amount of fluid $\mathcal{F}_C$ getting below the convection zone is negligible.

[5]This value changes by about a factor of 2 reflecting the luminosity increase during the time interval considered. We use the mean value in this estimate and remind the reader that $\dot{M}_e$ does not change in the same time interval, see Fig. 5. The contribution to $(\partial A/\partial t)_{conv}$ from mass entrainment is small and essentially the whole rate can be explained by energy generation in the convection zone.

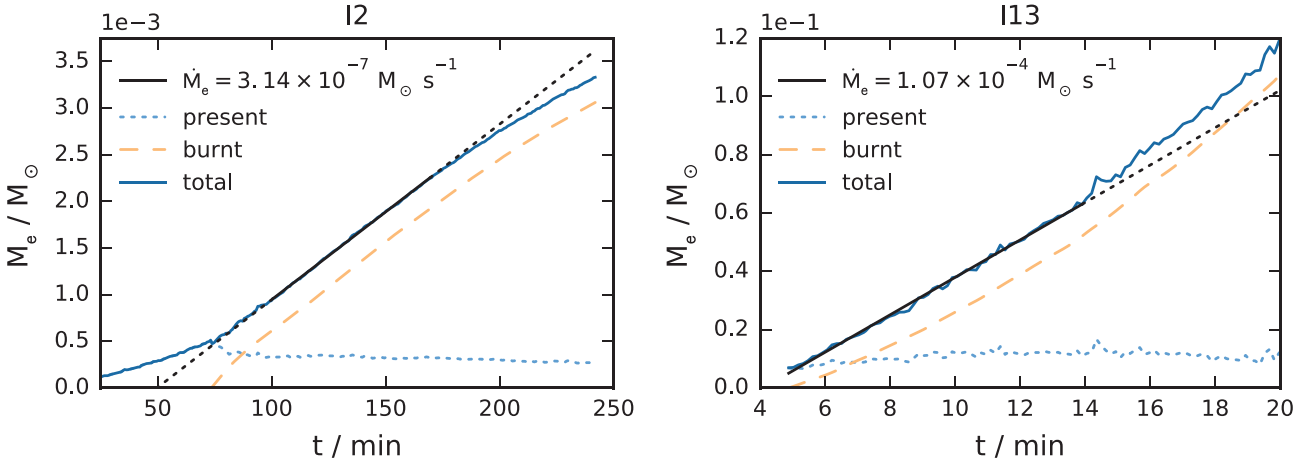

Figure 5. Total mass of fluid $\mathcal{F}_C$ that has been entrained into the convection zone is the sum of the mass of $\mathcal{F}_C$ currently present in the convection zone and the mass of $\mathcal{F}_C$ that has been burnt in the convection zone. The rate at which the total mass of $\mathcal{F}_C$ in the convection zone increases with time is the entrainment rate $\dot{M}_e$. In each panel, a linear fit to $M_e(t)$ is computed in the time interval where the black fitting line is solid; the dotted parts are to guide the eye. The deviations from the fitting line are discussed in Section 3.2. The luminosity driving convection is ∼150 × higher in run I13 [($f_{OO} = 67.5$), right-hand panel] as compared with I2 [($f_{OO} = 1$), left-hand panel], see Table 1.

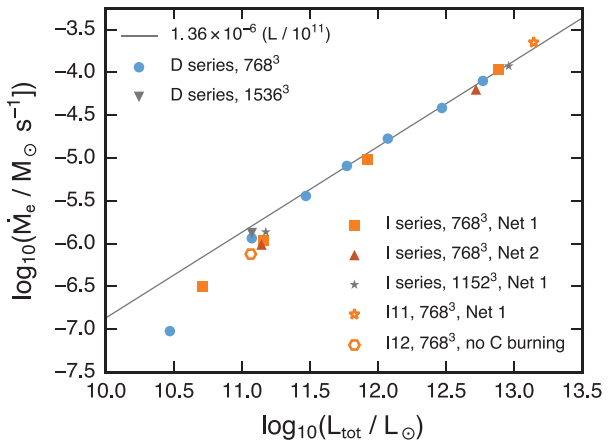

Figure 6. Dependence of the entrainment rate on the total luminosity L_{tot} integrated over the convection zone. A linear scaling law essentially identical to the one given in J17 is shown for comparison. The last 2.2 min of run I11 are used when the instability described in Section 3.6 has fully developed.

fig. 13 of J17). Nevertheless, their mass entrainment rate is in very good agreement with our scaling law (see fig. 19 of J17) despite some differences in the initial stratification.

3.3 Luminosity evolution

We calculate the global burning rates using spherically averaged profiles of density, temperature, and fractional volume of fluid $\mathcal{F}_C$ in a post-processing step. The spherically averaged rate of the $^{12}C + {}^{12}C$ reaction scales with $\langle X_{12}^2 \rangle = \langle X_{12} \rangle^2 + \sigma_{12}^2$, where σ_{12}^2 is the standard deviation of the distribution of X_{12} and the distribution is taken over the full solid angle at a constant radius. We first compute the rate of $^{12}C + {}^{12}C$ using $\langle X_{12} \rangle^2$ and then multiply the result by the factor $\xi = 1 + \sigma_{12}^2 / \langle X_{12} \rangle^2$, where σ_{12} is computed from the standard deviation of the fractional volume of fluid $\mathcal{F}_C$. In this way, we take into account the presence of ^{12}C clumps in the convection zone, which increases the resulting luminosity by a factor ranging from ∼1.2 in the least luminous runs to ∼2 in the most luminous ones compared to the luminosity calculated using the spherical average $\langle X_{12} \rangle$ only. The presence of clumps is a 3D effect and as such it is neglected in 1D stellar evolution calculations. The non-linear scaling of the $^{16}O + {}^{16}O$ reaction with the mass fraction X_{16} of ^{16}O is inconsequential as the fractional volume of fluid $\mathcal{F}_O$ deep in the convection zone is essentially unity at all times.

The average luminosities are computed for the time intervals during which the entrainment rates were measured (see Figs 5, B1, and B2), and they are summarized in Table 1. The time evolution of the luminosity contributions from O and C burning is shown in Fig. 7 for four characteristic cases. In the low-luminosity ($f_{OO} = 2.7$) run I4, the O-burning luminosity first decreases during the initial adjustment of the stratification and then it levels off. The C-burning luminosity ($^{12}C + {}^{12}C$) increases until an equilibrium is achieved between the rates of entrainment and burning with C burning providing ∼20 per cent of the total luminosity. The I16 case has the same O luminosity but it employs the C-burning network NET 2, which includes the $^{12}C + {}^{16}O$ reaction as well. This reaction dominates C burning when the concentration of ^{12}C in the convection zone is low as is the case in the low-luminosity runs I4 and I16. The contribution of C burning to the total luminosity is ∼17 per cent in I16.

Carbon burning is responsible for ∼33 per cent of the total luminosity in the more luminous run I13 ($f_{OO} = 67.5$, NET 1), but this fraction drops to ∼14 per cent when the reaction $^{12}C + {}^{16}O$ is included in the otherwise similar run I17 ($f_{OO} = 67.5$, NET 2), see Fig. 7. The reactions $^{12}C + {}^{12}C$ and $^{12}C + {}^{16}O$ are equally important in I17.

The luminosity L_C from the C-burning reactions makes up an increasingly larger fraction of the total luminosity L_{tot} as L_{tot} increases from run to run when burning network NET 1 is used, see Fig. 8. When 1152^3 runs were performed the L_C/L_{tot} fractions agree with the corresponding 768^3 runs. Because we start our analysis when a quasi-stationary state has been reached (with the exception of the unstable run I11), L_C is close to $q X_{12} \dot{M}_e$, where q is the energy released per unit mass of ^{12}C burnt and $X_{12} = 0.13$ the mass fraction of ^{12}C in the entrained material (see Section 2.2.2). We can then write $L_C / L_{tot} = q X_{12} \dot{M}_e / L_{tot}$

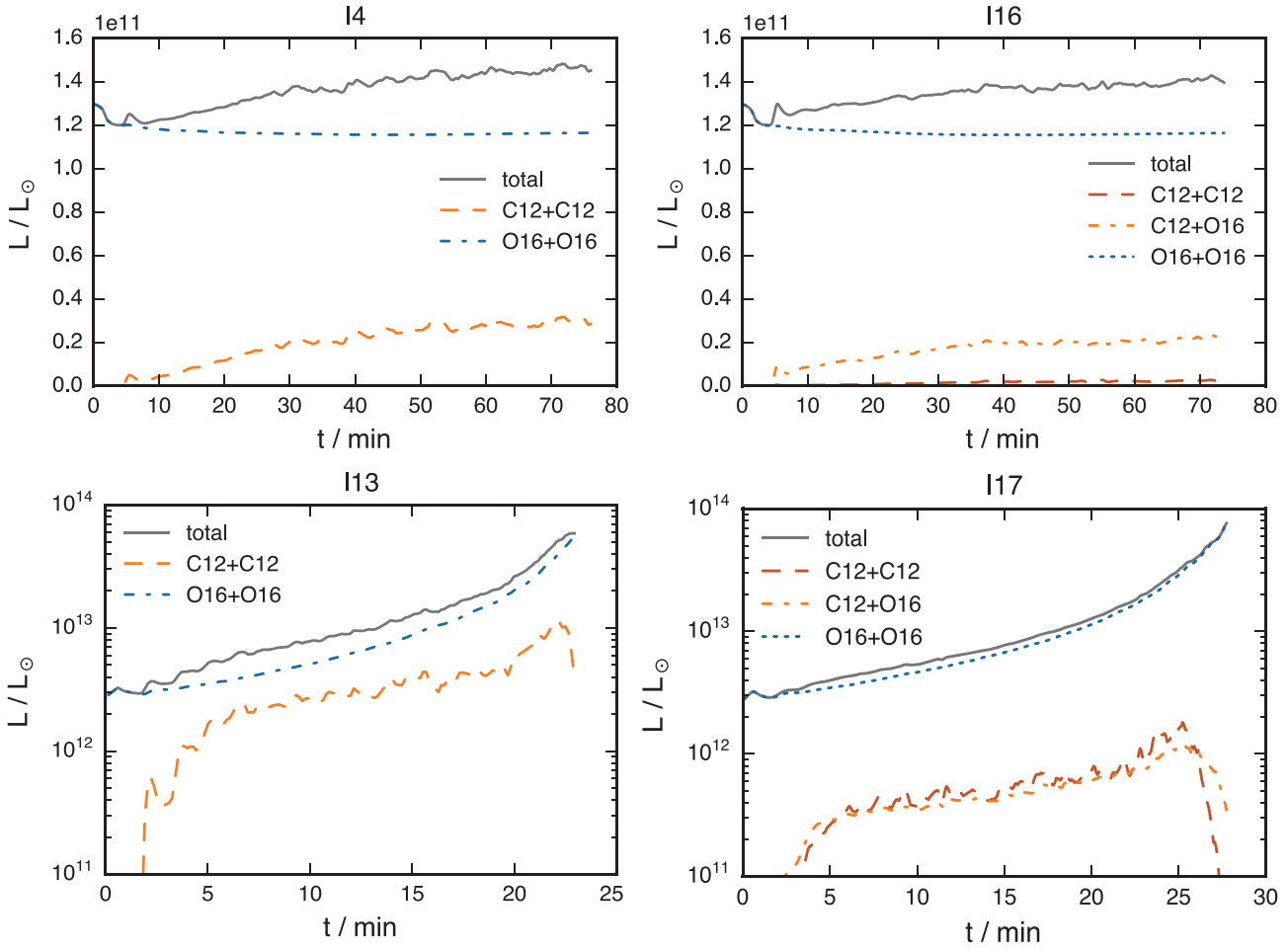

Figure 7. Time dependence of the contributions to the total luminosity integrated over the convection zone. The left two panels show runs I4 ($f_{OO} = 2.7$) and I13 ($f_{OO} = 67.5$) with the burning network NET1 ($^{12}C + {}^{12}C$) and the two panels on the right shown runs I16 ($f_{OO} = 2.7$) and I17 ($f_{OO} = 67.5$), which use NET2 ($^{12}C + {}^{12}C$ and $^{12}C + {}^{16}O$, see Section 2.2.4 for details).

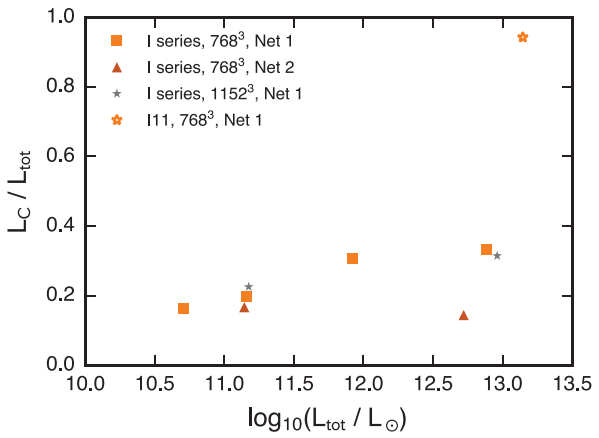

Figure 8. Dependence on the total luminosity of the fraction L_C/L_{tot}, where L_C is the luminosity from C-burning reactions and L_{tot} the total luminosity, both integrated over the convection zone. The last 2.2 min of run I11 are used when the instability described in Section 3.6 has fully developed.

with $\dot{M}_e/L_{tot} = 1.36 \times 10^{-17}\,M_\odot\,s^{-1}\,L_\odot^{-1}$ for all runs that follow the linear scaling relation shown in Fig. 6. The $^{12}C + {}^{12}C$ reaction as implemented in NET 1 has $q_{CC1} = 0.390\,MeV\,amu^{-1}$ (see Section 2.2.4), which implies $L_C/L_{tot} = 34.5$ per cent. This fraction is close to the measured values for runs I13 (33.3 per cent), I14 (31.4 per cent), and I5 (30.5 per cent), which closely follow the entrainment rate scaling. Runs with $L_{tot} \lesssim 3 \times 10^{11}\,L_\odot$ fall below the scaling relation in Fig. 6, which decreases $\dot{M}_e/L_{tot}$ and, consequently, also L_C/L_{tot} for these runs.

As implemented in NET 2, the yields of $^{12}C + {}^{12}C$ and $^{12}C + {}^{16}O$ reactions are $q_{CC2} = 0.133\,MeV\,g^{-1}$ and $q_{CO} = 0.438\,MeV\,g^{-1}$. The luminosities L_{CC} and L_{CO} due to the two reactions are almost equal in run I17 ($f_{OO} = 67.5$). The average yield, $q = 0.199\,MeV\,amu^{-1}$, is almost 2 × lower than that in the otherwise similar run I13 ($f_{OO} = 67.5$, NET 1), which explains the low value of L_C/L_{tot} in I17 as compared with I13 (see Fig. 8). Although C burning in run I16 ($f_{OO} = 2.7$, NET 2) is dominated by the $^{12}C + {}^{16}O$ reaction, the average yield $q = 0.358\,MeV\,amu^{-1}$ is comparable with $q_{CC1} = 0.390\,MeV\,amu^{-1}$ of $^{12}C + {}^{12}C$ (NET 1) used in the otherwise similar runs I4 and I15 ($f_{OO} = 2.7$). Fig. 8 confirms that L_C/L_{tot} reaches comparable values in runs I4, I15, and I16 ($L_{tot} \sim 1.5 \times 10^{11}\,L_\odot$).

An interesting feature of all of the I-series runs with $L_{tot} \gtrsim 3 \times 10^{12}\,L_\odot$ is that their luminosity significantly increases in time. This is due to the gradual heating up of the convection zone (by ∼10 per cent) combined with the nuclear reactions' high-temperature sensitivity: quantified as $\partial \log \varepsilon / \partial \log T$, the typical sensitivities at the bottom of the convection zone are 32 for $^{16}O + {}^{16}O$, 19 for $^{12}C + {}^{12}C$, and 25 for $^{12}C + {}^{16}O$.

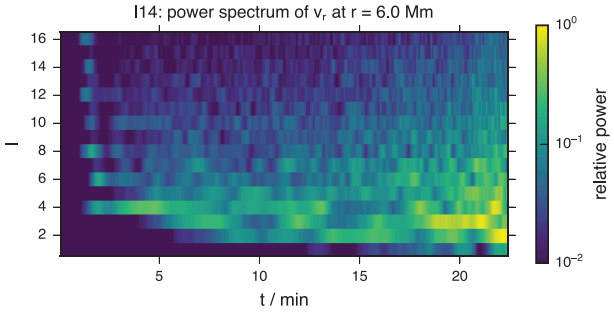

Figure 9. Spherical harmonic power spectrum of the radial velocity component v_r at $r = 6$ Mm in run I14 ($f_{OO} = 67.5$) shown as a function of time.

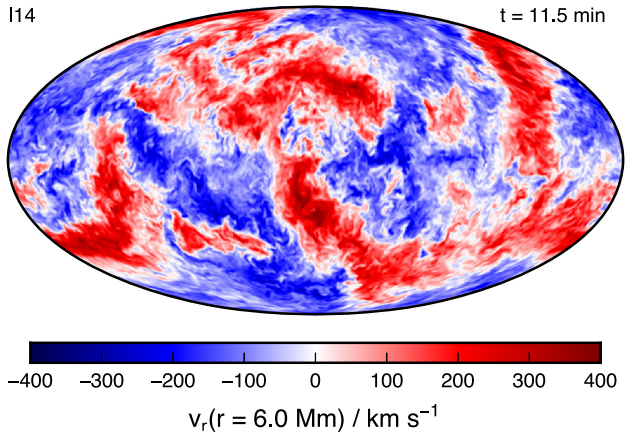

Figure 10. Typical distribution of the radial velocity v_r at $r = 6$ Mm. Run I14 ($f_{OO} = 67.5$) is shown in the equal-area Mollweide projection at $t = 11.5$ min. The rendering is based on a full 3D data cube downsampled from the run's resolution 1152^3 to 288^3.

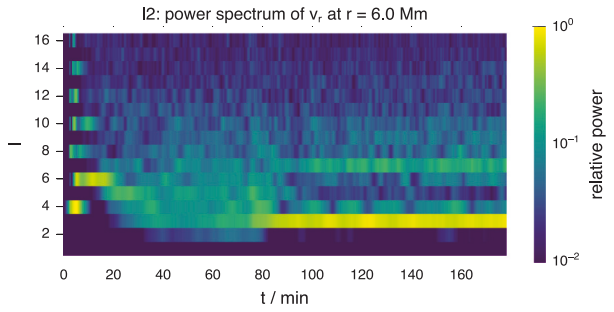

Figure 11. As Fig. 9 but run I2 ($f_{OO} = 67.5$) is shown.

3.4 Velocity field

To construct the initial condition, we map a 1D hydrostatic stratification on to a 3D Cartesian grid and set all velocity components to zero. The convective flow is driven by the heat released from O burning at the bottom of the shell. An initial transient flow carrying an imprint of the computational grid disintegrates rapidly and the flow becomes fully turbulent after a few convective overturns as described in detail by Woodward et al. (2015) and Jones et al. (2017). This effect can also be seen in the radial velocity spectra shown in Figs 9 and 11, in which an initially regular pattern of modes quickly disappears and is replaced by a turbulent spectrum.

It is difficult to quantify the degree of turbulence in our simulations in terms of a Reynolds number, because the PPM advection scheme does not include any explicit viscous term and its implicit viscosity depends strongly on the ratio $\lambda/\Delta x$ of the wavelength λ of interest in the velocity field and the grid cell width Δx. Porter & Woodward (1994) measure the dissipation properties of PPM and derive the Reynolds number

$$\mathrm{Re}_{\max} = \frac{4\pi^2}{A_s}\left(\frac{\lambda}{\Delta x}\right)^3 \tag{5}$$

associated with structures on the wavelength λ, where the coefficient A_s depends on the Courant number $\mathrm{Ca} = v\Delta t/\Delta x$. For run I4 ($f_{OO} = 2.7$) we have a typical rms convective velocity $v = 40\,\mathrm{km\,s^{-1}}$ and time-step $\Delta t = 3.8 \times 10^{-3}$ s, which gives $\mathrm{Ca} = 6.0 \times 10^{-3}$ for the advection of a typical fluid parcel. We estimate $A_s = 47$ for this value of Ca based on Table 1 of Porter & Woodward (1994). The relevant length-scale λ in our O shell is the depth of the shell, which is 4.0 Mm or 157 computational cell widths on the 768^3 grid. Equation (5) then gives $\mathrm{Re}_{\max} = 3.2 \times 10^6$. For the 1536^3 grid (run D2), the Reynolds number would be $(1536/768)^3 = 8$ times larger: $\mathrm{Re}_{\max} = 2.6 \times 10^7$. These large values, although still many orders of magnitude smaller than what one would expect for the stellar interior, reflect the low effective viscosity of the PPM scheme on the largest flow scales. Sytine et al. (2000) show that the spectrum of 3D PPM turbulence is almost indistinguishable from the expected Kolmogorov scaling for structures with a wavelength of 32 grid cells or more, which is 1/5 of the depth of our convective shell on the 768^3 grid. Strong dissipation sets in for wavelengths smaller than about 6 grid cells or 4 per cent of the shell's depth.

Fig. 10 shows that the velocity field is dominated by large-scale updraughts and downdraughts with complex small-scale turbulent structure in the state of quasi-stationary convection. The velocity distribution changes randomly in time and no particular direction in space is preferred, as expected of convection in the absence of rotation and magnetic field. The large-scale flow pattern remains essentially the same when grid resolution is increased from 768^3 to 1152^3.

Several low-order modes, including an $l = 2$ mode, make approximately equal contributions to the velocity field in most of our intermediate- and high-luminosity runs, see runs I5 ($f_{OO} = 13.5$, NET 1) and I13 ($f_{OO} = 67.5$, NET 1) in Fig. C1 and I14 ($f_{OO} = 67.5$, NET 1) in Fig. 9. The high-luminosity run I17 ($f_{OO} = 67.5$, NET 2) is an exception discussed below. A strong dipolar component ($l = 1$), which one would not expect in stationary convection in a shell with an inner radius as large as one-half of its outer radius, only appears towards the end of run I11, which shows a very asymmetric instability (see Section 3.6) reminiscent of the GOSH phenomenon (Herwig et al. 2014). A contribution from an $l = 1$ mode is present in the high-luminosity runs I13 and I14, but it is small and it only develops when a large portion of the upper stable layer has been entrained and the upper boundary of the convection zone approaches the outer boundary condition.

We observe a weak but noteworthy effect in low-luminosity runs I2 ($f_{OO} = 1$, NET 1), I4 ($f_{OO} = 2.7$, NET 1), I12 ($f_{OO} = 2.7$, no C burning), I15 ($f_{OO} = 2.7$, NET 1), and I16 ($f_{OO} = 2.7$, NET 2). The large-scale flows keep changing their distribution for $\sim$10–15 overturning time-scales, after which they start to converge towards the $l = 3$ mode of order $m = -2$ with large-scale updraughts and downdraughts aligned with the diagonals of the simulation cube. The flow remains highly turbulent and it is sometimes difficult to recognize this pattern by eye, but it can nevertheless be identified using spherical harmonic analysis (Fig. 11) and visualized by

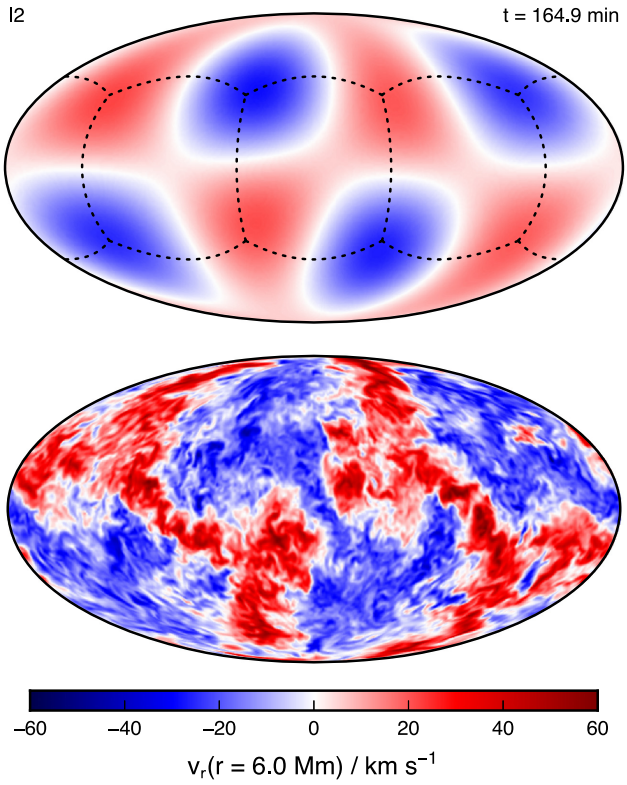

Figure 12. Distribution of the radial velocity v_r at $r = 6$ Mm and $t = 164.9$ min in run I2 ($f_{OO} = 67.5$, see also Fig. 11). The top panel only shows spherical harmonic components of degree $l \leq 4$ based on averages in 80 triangular patches covering the sphere ('buckets', see Section 2.2.1). This pattern, close to the spherical harmonic mode of degree $l = 3$ and order $m = -2$ and clearly aligned with the corners of the simulation cube (dashed lines), occurs when the driving of convection is very weak.[6] Smaller scales in the velocity field can be seen in the bottom panel, which is based on a full 3D data cube downsampled from the run's resolution 768^3 to 192^3. The equal-area Mollweide projection is used in both maps.

applying a low-pass filter to the velocity distribution (Fig. 12). It is suspicious that the grid aligned pattern first appears at $t \approx 80$ min in I2, because we turned on C burning in that run at $t = 74$ min, see Section 2.2.3. However, we see the same pattern in runs I4, I15, and I16 that had C burning on from $t = 0$ and even in run I12 that had C burning turned off throughout. It is possible that the geometry of our shell slightly prefers convection cells about as large as those of an $l = 3$ mode and, if the convection is weakly driven, these cells align themselves with the $l = 3$ mode that is slightly preferred by our Cartesian grid. We are currently investigating such subtle effects that occur in slow flows using a new version of the PPMSTAR code, which solves for fluctuations around a base state. Our preliminary results indicate that this formulation offers advantages for problems involving weakly driven convection.

Since the grid-alignment occurs in the phase of quasi-stationary convection, one might suspect that this effect could somehow influence the entrainment rate, which we measure in this phase, and it could possibly explain why the entrainment rates are lower than what our scaling law predicts at low luminosities, see Section 3.2 and Fig. 6. However, we find that the entrainment rate slightly increases in the early evolution towards the quasi-stationary state in all of the relevant runs, see run I2 ($f_{OO} = 1$, NET 1) in Fig. 5, I4 ($f_{OO} = 2.7$, NET 1) in Fig. B1, and runs I15 ($f_{OO} = 2.7$, NET 1) and

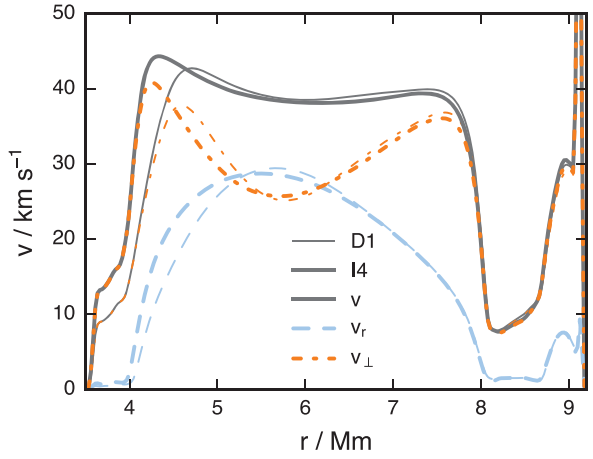

Figure 13. Total (v), radial (v_r), and tangential ($v_\perp$) rms velocities in run I4 ($f_{OO} = 2.7$) as compared with run D1 of J17.

I16 ($f_{OO} = 2.7$, NET 2) in Fig. B2. Therefore, if the grid-alignment effect has any influence on the entrainment rate, it most likely causes a slight increase and not a decrease.

Our choice of the C-burning network (NET 1 versus NET 2) does not influence the velocity distribution at the low luminosity of runs I4 ($f_{OO} = 2.7$, NET 1) and I16 ($f_{OO} = 2.7$, NET 2). Velocity spectra from these two runs are essentially the same, see Fig. C1. This is not the case for the pair of high-luminosity runs I13 ($f_{OO} = 67.5$, NET 1) and I17 ($f_{OO} = 67.5$, NET 2). I13 switches between modes $l = 2$, 3, 4 at random whereas I17 is dominated by an $l = 3$ mode throughout most of it evolution. Convection cells in this pattern, however, keep moving around the sphere unlike those in the low-luminosity runs mentioned above. We do not know the cause of this effect.

The fact that we use a realistic O-burning prescription and include the burning of the entrained material in our simulations as opposed to the simulations presented by J17 makes surprisingly little difference for time-averaged velocity profiles. Fig. 13 compares the low-luminosity run I4 ($f_{OO} = 2.7$) with the similar run D1 of J17. The only difference can be seen at the transition from the lower stable layer into the convection zone, which is located deeper and is more abrupt in I4 than in D1. This is qualitatively compatible with the heating rate distribution's being more concentrated to the bottom of the convection zone in the I series of runs, see Figs 2 and 4. We can see the same effect in the comparison between the high-luminosity runs D10 and I13 ($f_{OO} = 67.5$) in Fig. 14.

Convective velocity is expected to scale with $L_{tot}^{1/3}$ on theoretical grounds (Biermann 1932; Porter & Woodward 2000; Müller & Janka 2015; J17), where L_{tot} is the total luminosity driving convection. We calculate the rms velocity $v_{rms} = (2E_{k,cz}/M_{cz})^{1/2}$, where $E_{k,cz}$ and M_{cz} are the total kinetic energy and mass of the convection zone, respectively. We average v_{rms} over the time interval during which the entrainment rate is measured, see Figs 5, B1, and B2. Fig. 15 shows that all runs, including the unstable run I11 (see Section 3.6 for details), closely follow the expected scaling law and only the least luminous run D23 starts to deviate from it (by ∼16 per cent).

3.5 Fluctuations

The 3D, time-dependent nature of the flow gives rise to a whole spectrum of fluctuations. Their magnitude depends on the total luminosity, which both determines and depends on the entrainment

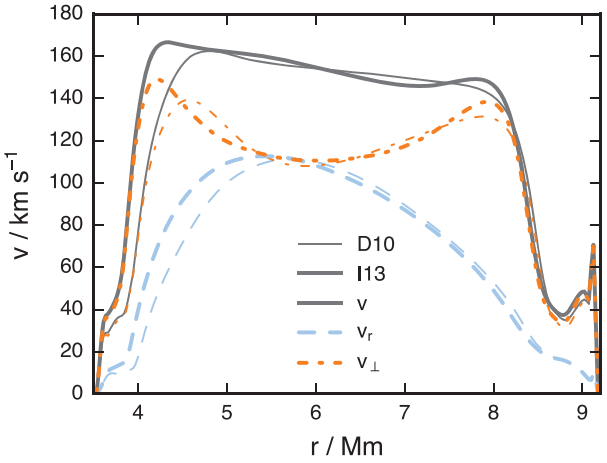

Figure 14. As Fig. 13, but runs I13 ($f_{OO} = 67.5$) and D10 are shown.

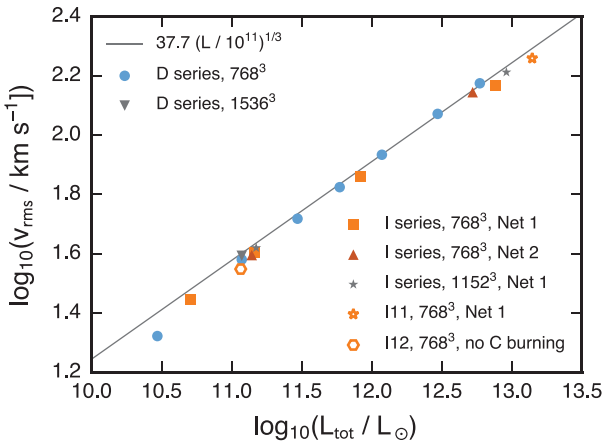

Figure 15. Dependence of the rms convective velocity v_{rms} on the total luminosity L_{tot} integrated over the convection zone. The expected scaling law $v_{rms} \propto L_{tot}^{1/3}$ is shown for comparison. The last 2.2 min of run I11 are used when the instability described in Section 3.6 has fully developed.

rate. To quantify these fluctuations, we have used averages measured in 80 different directions ('buckets', see Section 2.2.1 for details).

Fig. 16 compares the low-luminosity run I2 ($f_{OO} = 1$) with the high-luminosity run I13 ($f_{OO} = 67.5$) in terms of the relative rms fluctuations $X'_{rms}(r)/X(r)$, where X is the quantity of interest, $X(r)$ the spherical average of X at the radius of r, and

$$X'_{rms}(r) = \sqrt{\frac{1}{N}\sum_{i=1}^{N}[X_i(r) - X(r)]^2}, \quad (6)$$

defines the absolute rms fluctuations, where $N = 80$ is the total number of buckets. Fluctuations in the density ρ, pressure p, and temperature T are the same within a factor of a few in the convection zone and they increase with increasing luminosity. Pressure fluctuations are much smaller than density fluctuations in the stable layers as expected for buoyancy-driven internal waves.

Density fluctuations in the convection zone are close to Ma^2 in both I2 and I13 (see Table 1 for the Ma values). The contrast in magnitude between the density and temperature fluctuations at the convective boundaries and those in the convection zone becomes larger with decreasing luminosity and Mach number. Meakin & Arnett (2007a) estimate the magnitude of density fluctuations in a

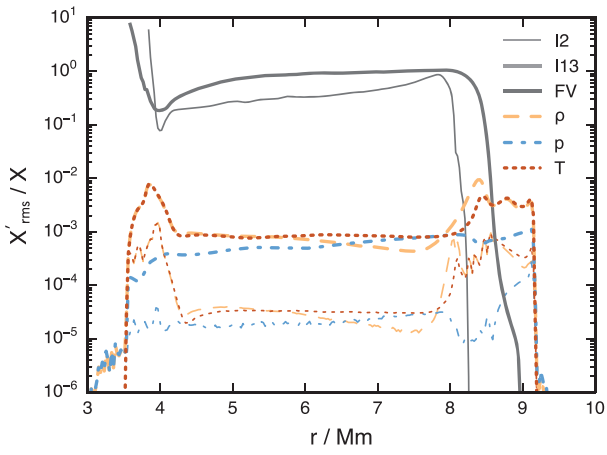

Figure 16. Relative large-scale rms fluctuations of the fractional volume FV of fluid $\mathcal{F}_C$, density ρ, pressure p, and temperature T as determined from 80 radial *buckets* that together cover the full solid angle (see Section 2.2.1 for details). Runs I2 ($f_{OO} = 1$, NET 1) and I13 ($f_{OO} = 67.5$, NET 1) are shown at $t = 134.9$ min and $t = 9.32$ min, respectively, when I13 is ∼150 times more luminous than I2.

convection zone and at its boundaries as $\rho'/\rho \sim Ma^2 + v_{conv}\,N/g$, where Ma is the convective Mach number, v_{conv} the convective velocity, N the local Brunt–Väisälä frequency, and g the gravitational acceleration. The $v_{conv}\,N/g$ term is proportional to Ma, so the relative magnitude of density fluctuations in the stable layers as compared to those in the convection zone is inversely proportional to Ma (cf. Fig. 16). Both convective boundaries in our simulations are characterized by approximately the same ratio $g/N \approx 4500$ km s^{-1}. Substituting v_{rms} from Table 1 for v_{conv}, we get that the contribution to ρ'/ρ from the term $v_{conv}\,N/g = v_{conv}/(g/N)$ in the expression above is $\approx 6 \times 10^{-3}$ in I2 and $\approx 3 \times 10^{-2}$ in I13. These values are significantly larger than our measurements shown in Fig. 16, which implies that the order-of-magnitude expression $v_{conv}\,N/g$ overestimates the actual fluctuations on the bucket-to-bucket scale.[7]

We plot the uncorrected temperature T in Fig. 16, although nuclear reaction rates are computed using the corrected temperature Θ (equations 2 and 3). Fig. 17 shows relative fluctuations in Θ close to the end of run I14 (one of the most luminous, $f_{OO} = 67.5$). They are smaller than 1 per cent, which limits their possible influence on the C-burning rates to $\lesssim 20$ per cent even at the upper end of the luminosity range considered (see Section 3.3 for the reactions' temperature sensitivities). For this reason, we did not include them in Fig. 3.

Fluctuations in the fractional volume FV of fluid $\mathcal{F}_C$ are large in all of our runs, including the least luminous ones (see Fig. 16 and also Fig. 3). They slightly increase with increasing luminosity, although much less than the fluctuations in ρ, p, and T do, and they create large-scale asymmetries in the energy generation rate as shown in Fig. 3. The FV fluctuations in runs I16 ($f_{OO} = 2.7$) and I17 ($f_{OO} = 67.5$), which use the C-burning network NET 2, are larger than those in a similar pair of runs I4 ($f_{OO} = 2.7$) and I13 ($f_{OO} = 67.5$), in which NET 1 is used, see Fig. 18. This is likely a consequence of the fact that a certain concentration X_{12} of ^{12}C has to first build up in the convection zone to make the time-scale of

[7]We have sub-bucket-scale rms information for the fractional volume only, but it is not included in Fig. 16 for consistency with the other variables shown.

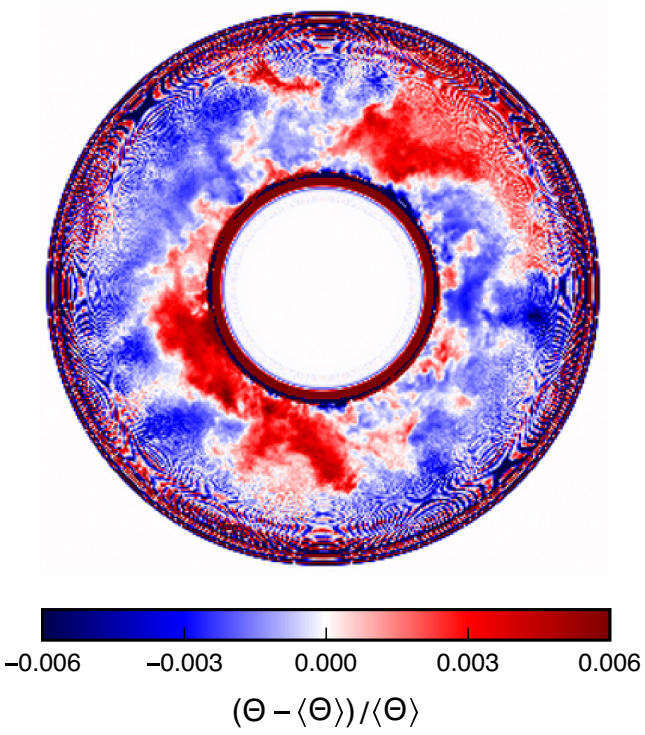

Figure 17. Relative fluctuations in the corrected temperature Θ (see equation 3 and Section 2.2.4) with respect to the spherical average $\langle\Theta\rangle$ at $t =$ 21.3 min in run I14 ($f_{OO} = 2.7$). The fluctuations are averaged over an XZ slice 1 Mm thick (5 per cent of the simulation box width). The rendering is based on data downsampled from 1152^3 to 288^3 that were further subject to a lossy compression algorithm (see Section 2.2.1 for details). Numerical noise from the compression step dominates the outer portion of the rendering.

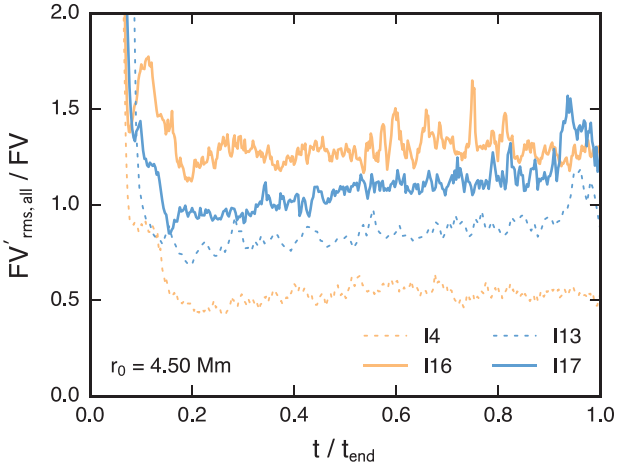

Figure 18. Time evolution of the relative rms fluctuations in the fractional volume FV of fluid $\mathcal{F}_C$ at the radius of $r_0 = 4.5$ Mm in runs I4 ($f_{OO} = 2.7$, NET 1), I13 ($f_{OO} = 67.5$, NET 1), I16 ($f_{OO} = 2.7$, NET 2), and I17 ($f_{OO} =$ 67.5, NET 2). All spatial scales are considered here as opposed to Fig. 16. Simulation time on the abscissa is normalized for clarity.

the $^{12}C + {}^{12}C$ reactions ($\propto X_{12}^{-1}$) considered in NET 1 short enough to balance the rate of mass entrainment whereas the C-burning time-scale is independent of X_{12} for the $^{12}C + {}^{16}O$ reactions that are also included in NET 2. $^{12}C + {}^{16}O$ reactions are responsible for ∼50 per cent of the C-burning luminosity in run I17 and they

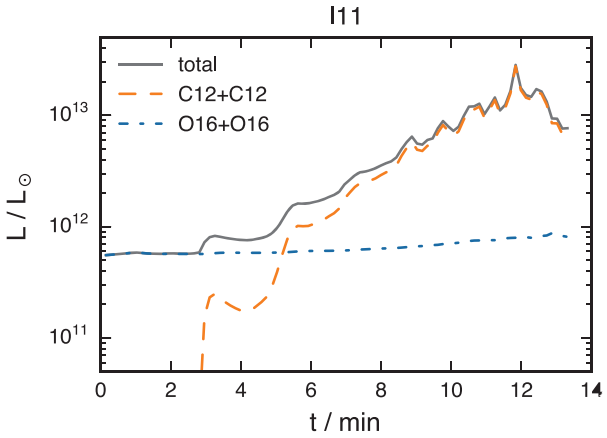

Figure 19. Contributions to the total luminosity integrated over the convection zone in run I11 ($f_{OO} = 13.5, f_{CC} = 10$).

dominate C burning in run I16, see Section 3.3. The FV fluctuations as quantified in Fig. 18 are slightly larger than those in Fig. 16 (compare run I13 shown in both), because all spatial scales are considered (i.e. the index i in equation 6 runs over computational grid cells instead of the buckets) in Fig. 18 as opposed to Fig. 16.

3.6 Instability in a case with strong feedback as in O–C shell merger conditions

Depending on the entropy difference between a pair of interacting O- and C-burning convective shells, the rate of mass entrainment into the O shell and the corresponding feedback from C burning could be even larger than in the simulations discussed so far. In terms of the nucleosynthetic signature of the O–C shell merger, Ritter et al. (2018a) show that the production of odd-Z elements increases with increasing entrainment rate and mixing efficiency, and they suggest that the largest enhancements could be reached in a case in which the O and C shells merge completely on the dynamical time-scale. An entrainment rate of $\sim 1\ M_\odot\ s^{-1}$ could be reached assuming near-sonic mass exchange, which we consider an upper limit. To explore this regime within the framework of the current series of runs, we have carried out a variation of the medium-luminosity run I5 ($f_{OO} =$ 13.5) which has an entrainment rate of $\sim 10^{-5}\ M_\odot\ s^{-1}$. In order to mimic the energy feedback encountered in a situation closer to a complete merger, we increase the energy yield of C burning by the factor $f_{CC} = 10$ in run I11. Even taking into account that we increased the amount of C in the ingested material by a factor of 5 compared to the stellar model value (Section 2.2.2), the resulting entrainment rate (see below), which sets the strength of the energy feedback, stays well below the above-mentioned upper limit. The degree of asymmetric perturbations reported in this section for run I11 may therefore be considered as a lower limit for the case of a complete O–C shell merger.

Fig. 19 shows that the C-burning luminosity ($^{12}C + {}^{12}C$) starts rapidly increasing soon after the onset of entrainment in I11. C burning quickly becomes the dominant source of energy and exponential growth ensues. Strong, large-scale oscillations akin to the GOSH phenomenon described by Herwig et al. (2014) develop after $t \approx 11$ min. In terms of spherical harmonics, modes with $l =$ 1 to $l = 4$ are dominant (see Fig. 20) and the upper convective boundary gets significantly deformed (see Fig. 21). The oscillations can also be seen in Fig. 22, which shows at four points in time the Mach numbers Ma_r and $Ma_\perp$ corresponding to motions in the

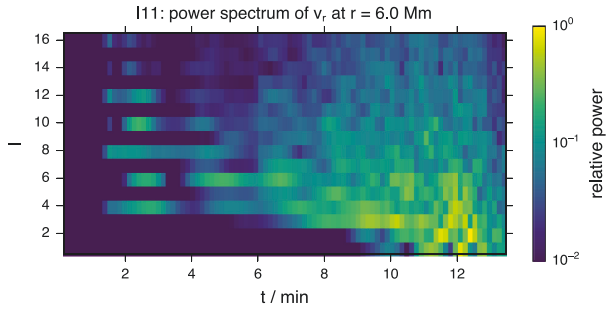

Figure 20. Time evolution of the spherical harmonic power spectrum of the radial velocity v_r at the radius of 6 Mm in run I11 ($f_{OO} = 13.5, f_{CC} = 10$). Spectral power is normalized by its maximum value.

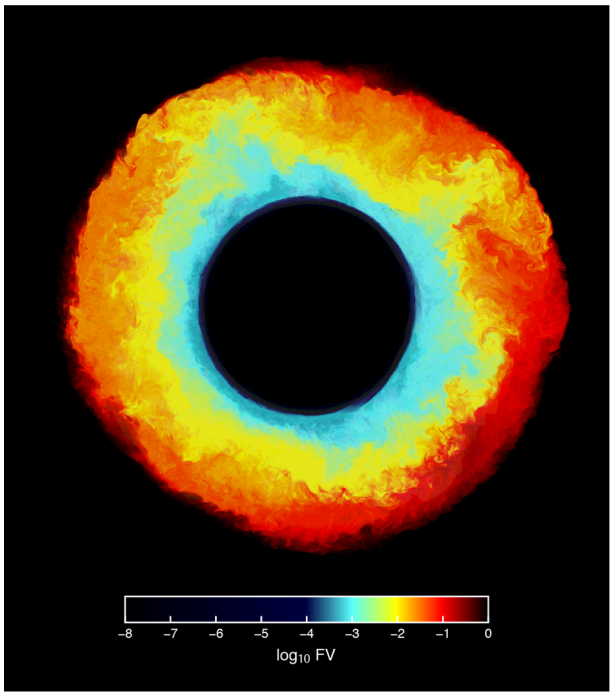

Figure 21. Rendering of the fractional volume of fluid $\mathcal{F}_C$ in a thin slice through the computational box at $t = 12.6$ min in run I11 ($f_{OO} = 13.5, f_{CC} = 10$).

radial and tangential direction, respectively, and the relative density fluctuations $(\rho - \langle\rho\rangle)/\langle\rho\rangle$. High values of Ma_r and $Ma_\perp$, reaching ∼0.3 locally, are concentrated to one-half of the renderings at $t = 10.9$ min and at $t = 12.0$ min. The density fluctuations follow the same pattern. They reach values up to ∼15 per cent in some parts of the upper boundary due to the boundary's large-scale deformation, but they also approach 5 – 10 per cent in the bulk of the convection zone at $t = 12.0$ min. The Courant number exceeds unity at some point in the simulation volume at $t = 13.5$ min and the simulation is stopped. Fig. 22 also shows that although the convective boundary is well separated from the outer spherical wall boundary condition during the initial growth of the instability, some parts of the flow reach the outer wall by $t = 12$ min and are likely to be influenced by its presence at the end of the run. This results from this run's being more violent than anticipated.

Our standard method of determining the entrainment rate is not applicable to cases of very violent convection associated with strong motions in the upper stable layer as mentioned in Section 3.2. In order to characterize the entrainment process throughout run I11, we have slightly modified this method. Instead of using the average velocity profile to define the upper boundary of the convection zone, we use the bucket data (see Section 2.2.1) to measure the radius of the boundary using fractional volume profiles of fluid $\mathcal{F}_C$ in 80 different directions. We define the radius of the upper boundary in each individual bucket as the largest radius inside that the fractional volume does not exceed $\frac{1}{2}$ and we integrate the amount of fluid $\mathcal{F}_C$ inside that radius. We have compared this method with that described in Section 3.2 in the time interval from 6.2 to 9.3 min, in which both methods are applicable. Our standard method yields $\dot{M}_e = 3.07 \times 10^{-5}\,M_\odot\,s^{-1}$ in this time interval. With the new method, we obtain $\dot{M}_e = 3.61 \times 10^{-5}\,M_\odot\,s^{-1}$, i.e. a value only 18 per cent larger. The new method allows us the measure the ultimate entrainment rate achieved in the last 2 min of run I11: $\dot{M}_e = 2.24 \times 10^{-4}\,M_\odot\,s^{-1}$, see Fig. 23.

This entrainment rate is similar to the 1D nucleosynthesis run Sm4 of Ritter et al. (2018a) that produces only modest enhancements of odd-Z elements. It is also similar to our high-luminosity runs I13 and I14 ($f_{OO} = 67.5$, no C-burning enhancement), which do not show the runaway effect observed in I11. Although mass entrainment and the subsequent nuclear burning are not spherically symmetric in any of our 3D runs, the use of a 1D mixing prescription for nucleosynthesis post-processing seems more justified in quasi-stationary cases like I13 or I14 than in the unstable case I11.

Although run I11 reaches a luminosity similar to that of runs I13, I14, and I17 (compare Fig. 19 with Figs 7 and A1), it differs from them qualitatively. Convection in the latter three runs is quasi-stationary and predominantly driven by O burning with O luminosity increasing on the time-scale of many convective overturns, following the heating up of the convection zone. The rates of change of the luminosity and entrainment rate are so rapid in I11 that this run cannot be considered quasi-stationary. Fig. 23 also shows that $M_e(t)$ in I11, unlike any in other run, is dominated by the entrained fluid's piling up in the convection zone. The total mass of fluid $\mathcal{F}_C$ entrained by the end of run I11 corresponds to only about 1/3 of the upper stable layer's initial mass whereas all of that layer gets ultimately entrained in runs I13, I14, and I17. The contribution of the temperature increase to the increase in the burning rates is rather limited in I11 as evidenced by the small ($\lesssim 50$ per cent) increase in the oxygen luminosity (see Fig. 19), which is a sensitive temperature indicator.

The behaviour of run I11 can be motivated as follows. The linearity of the dependence of the entrainment rate $\dot{M}_e$ on the total luminosity L_{tot} (see Fig. 6 and Section 3.2) suggests that the amount of energy needed to entrain a constant amount of mass is constant. The scaling relation gives $\dot{M}_{e,0} = 1.44 \times 10^{-6}\,M_\odot\,s^{-1}$ at $L_0 = 10^{11}\,L_\odot$, so $\Gamma = L_0/\dot{M}_{e,0} = 1.34 \times 10^{17}\,erg\,g^{-1}$, which can also be expressed as $\Gamma = 0.139\,MeV\,amu^{-1}$. Only the mass fraction $X_{C12} = 0.13$ of ^{12}C in the entrained fluid represents burnable fuel, so $\Gamma_{C12} = \Gamma/X_{12} = 1.07\,MeV\,amu^{-1}$ is the amount of energy needed to entrain one atomic mass unit of ^{12}C into the convection zone. Nuclear network NET 1 releases 9.35 MeV from every single $^{12}C + {}^{12}C$ reaction (24 amu of ^{12}C), which is $q_{CC} = 0.390\,MeV\,amu^{-1}$. Since $q_{CC} < \Gamma_{C12}$, the burning of the entrained material normally produces less energy than what was needed to entrain it.[8] We have, however, increased the energy release from NET 1 by the factor $f_{CC} = 10$ in run I11, so $f_{CC}\,q_{CC} = 3.90\,MeV\,amu^{-1} > \Gamma_{C12}$ holds for the amount of energy produced per unit mass of fuel burnt in this run. More

[8]This also holds for nuclear network NET 2.

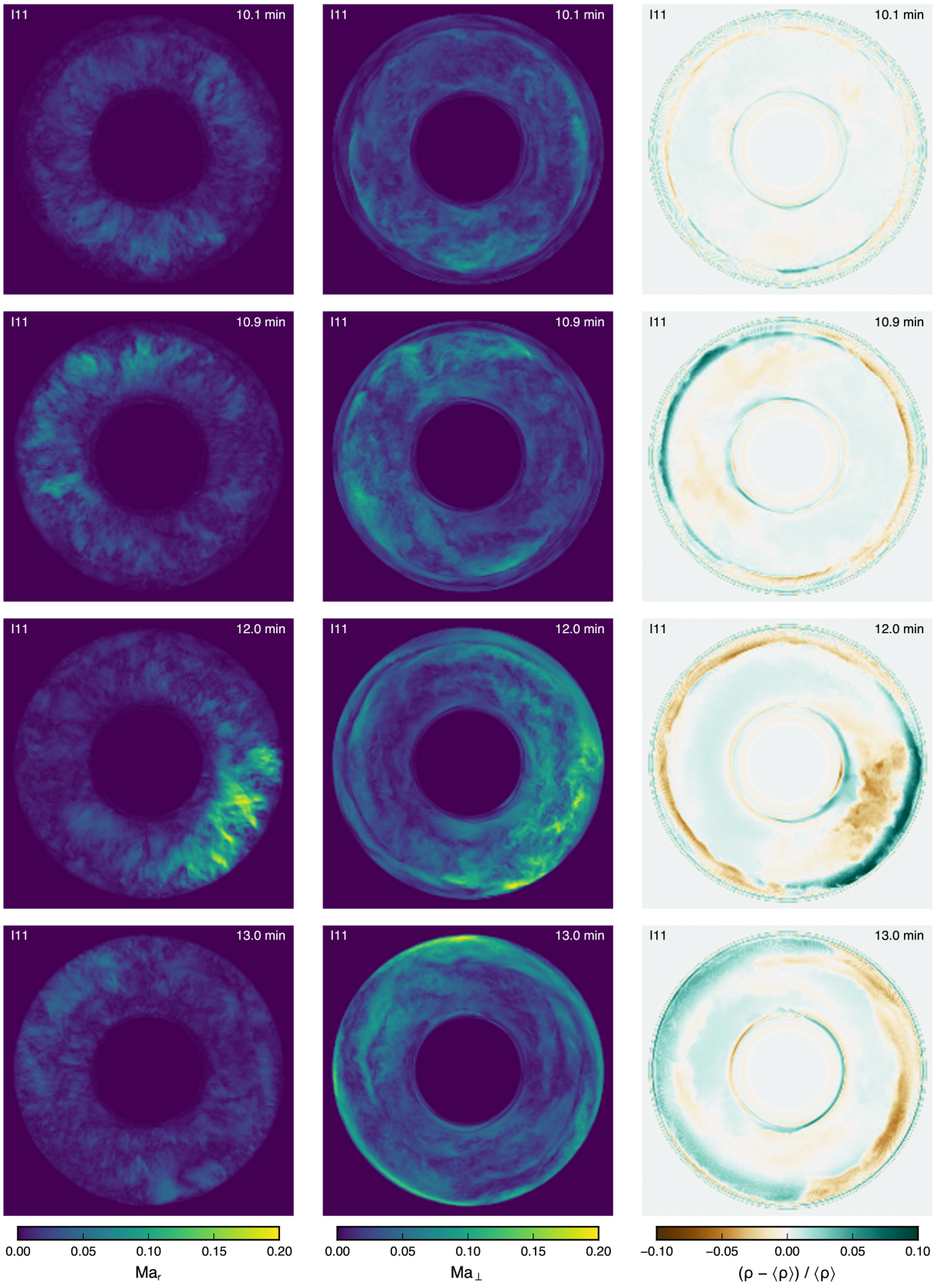

Figure 22. Time evolution of the Mach numbers $\mathrm{Ma_r}$ and $\mathrm{Ma_\perp}$ corresponding to motions in the radial and tangential direction, respectively, and of the relative density fluctuations $(\rho - \langle\rho\rangle)/\langle\rho\rangle$ in the last 3 min of run I11 ($f_{\mathrm{OO}} = 67.5, f_{\mathrm{CC}} = 10$).

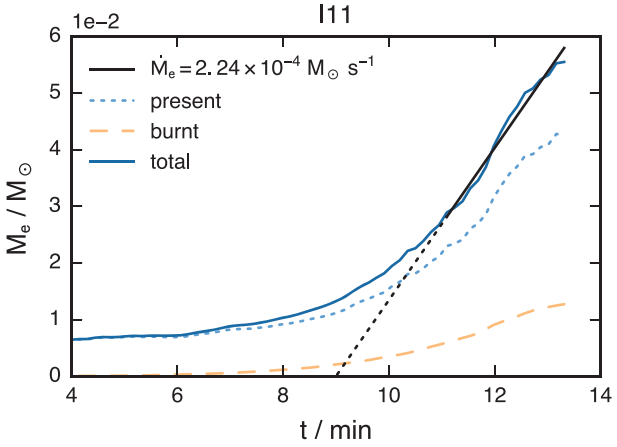

Figure 23. Like Fig. 5, but run I11 ($f_{OO} = 67.5, f_{CC} = 10$) is shown.

energy is produced from the burning of the entrained material than what was needed to entrain it. This closes a positive feedback loop that can explain the exponential growth seen in Figs 19 and 23.

The main caveat of this hypothesis is that the entrainment rate is rather slow to respond to changes in the total luminosity in other high-luminosity runs, see Section 3.2. The ε mechanism (see e.g. Kippenhahn et al. 2012) operating in the C-burning layer atop the convection zone may also contribute to the development of large-amplitude oscillations at the upper boundary, but the stability analysis involved in quantifying this contribution is beyond the scope of this paper.

4 SUMMARY AND CONCLUSIONS

We have employed 3D hydrodynamic simulations to investigate the dynamic feedback from the burning of a C-rich material ingested from a stably stratified layer into a convective O-burning shell in a model of an evolved massive star. All but one of the simulations reach a quasi-stationary state, in which the rates of mass entrainment and burning are in a close balance. Most of our runs use a 768^3 Cartesian grid, but two runs using a 1152^3 grid are in excellent quantitative agreement with their 768^3 counterparts (Figs 6, 8, and 15). This result provides further support for our previously established convergence upon grid refinement for the same setup (J17) as well as for other simulations performed using the PPMSTAR code (Woodward et al. 2015).

The entrainment rate $\dot{M}_e$ is proportional to the total luminosity, which in our suite of simulations spans almost three orders of magnitude (from $3 \times 10^{10}\,L_\odot$ to $\sim 10^{13}\,L_\odot$), although $\dot{M}_e$ starts to deviate from that scaling in the lowest third of the luminosity range. We suggest that these deviations might be caused by the low-luminosity simulations' being too short for convection to erode the initial transition layer between the two fluids and to form a new boundary consistent with the properties of the convection and of the entrainment process.

Carbon burning contributes between 16 per cent and 33 per cent of the total luminosity in the quasi-stationary state when only $^{12}C + {}^{12}C$ reactions are considered. $^{12}C + {}^{16}O$ reactions turn out to be equally important when the luminosity is high ($\sim 10^{13}\,L_\odot$) and they strongly dominate when the luminosity is low ($\lesssim 10^{11}\,L_\odot$). The contribution of C burning to the total luminosity is only $\sim$15 per cent almost independently of the luminosity when the network includes both $^{12}C + {}^{12}C$ and $^{12}C + {}^{16}O$ reactions. Because we assumed the concentration of ^{12}C in the fluid above the convection zone to be five times higher than that in the C shell of the particular MESA model that we started with, the feedback from C burning would likely be smaller still without that increase. This is the case in the simulations of Mocák et al. (2018), in which the concentration of ^{12}C above their O shell ranges from $\sim 10^{-5}$ to $\sim 10^{-4}$.

The velocity field is dominated by spherical harmonic modes $l = 2, 3, 4$, i.e. there are only a few large convective cells that start the turbulent cascade. The dominance of such global modes has been previously observed in simulations providing a full-solid-angle view of convection in similar environments, e.g. Bazan & Arnett (1994), Porter, Woodward & Jacobs (2000), Gilet et al. (2013), Jones et al. (2017), Müller et al. (2017). Mass entrainment occurs where these large-scale flows run into one another while turning over at the upper convective boundary and they start pulling slivers of the C-rich fluid downwards. Full-sphere simulations are therefore necessary to correctly quantify this process. The rms convective velocity scales with $L_{tot}^{1/3}$ as expected and the magnitude of velocity at any given total luminosity L_{tot} agrees with simulations of J17 who did not include O and C burning but instead used time-independent volume heating to drive convection in the shell.

Large-scale asymmetries in the distribution of the entrained C-rich material cause significant deviations of the burning rate from spherical symmetry. The quadratic dependence of the $^{12}C + {}^{12}C$ reaction rate on the mass fraction of ^{12}C enhances the C luminosity by up to a factor of two compared with an estimate based on spherical averages when this reaction dominates C burning. On the other hand, fluctuations in the density, pressure, and temperature are smaller than 1 per cent in the convection zone proper. The only exception is run I11, in which we experimentally increased the energy release from our simple C-burning network by a factor of ten to explore the regime closer to a full, dynamic-time-scale merger of the O and C shells. An exponentially growing instability starts immediately after the onset of C entrainment in I11 and density fluctuations reach $\sim$5 per cent in the convection zone when a dipolar oscillation has developed in the flow field with a Mach number locally exceeding 0.2. Fluctuations of such magnitude are known to facilitate shock revival in supernova explosion simulations (Couch & Ott 2013, 2015; Müller & Janka 2015; Müller et al. 2017). If such an instability occurs well before core collapse it might power an SN impostor event assuming that there is a physical mechanism capable of transporting a significant fraction of the kinetic energy contained in the O shell ($\sim 3 \times 10^{47}$ erg for $v_{rms} \sim 200\,km\,s^{-1}$) to the star's extended envelope. The entrainment rate reached in the instability, $2 \times 10^{-4}\,M_\odot\,s^{-1}$, is close to what is needed to obtain significant production of the odd-Z elements Cl, K, and Sc according to the nucleosynthesis calculations of Ritter et al. (2018a). Still, the energy feedback from C ingestion in case I11 is smaller than the energy feedback expected due to the maximum entrainment rate that may be encountered in a full, dynamic O–C shell merger.

We show in Section 3.6 that the instability in run I11 could have been caused by the fact that more energy was released from the burning of one unit of entrained mass in I11 than what was needed to entrain that mass. Although this is a direct consequence of our having increased the energy release from C burning in this run, there are a number of energy producing reactions that our simple nuclear network does not include, e.g. those caused by the products of C burning or by the burning of ^{20}Ne that is abundant in the C shell. Our energy argument suggests that the instability would also occur with less feedback from the burning if the entrainment rate was larger at the same luminosity, which would likely happen if we considered an O shell with a softer upper boundary. Finally, interaction between

the convective flows in merging O and C shells (the latter not considered in this work) could contribute to the development of instabilities at the interface as well.

Animated visualizations of some of the simulations presented in this work are available on Zenodo.org[9] and on YouTube.[10] Readers interested in analysing the 3D data sets presented in this paper are encouraged to contact the authors who can provide JupyterHub data exploration access via the Astrohub[11] platform.

ACKNOWLEDGEMENTS

RA, who completed most of this work as a CITA (Canadian Institute for Theoretical Astrophysics) national fellow, acknowledges support from CITA and from the Klaus Tschira Stiftung. PW acknowledges NSF (National Science Foundation) grants 1413548 and 1515792. FH acknowledges support from a NSERC (National Sciences and Engineering Research Council) Discovery grant. This research was conducted as part of the JINA (Joint Institute for Nuclear Astrophysics) Center for the Evolution of the Elements (NSF grant PHY-1430152). NCSA's (National Center for Supercomputing Applications') Blue Waters and Compute Canada/WestGrid provided the computing and data processing resources for this project. We thank two anonymous referees for their comments, which improved the quality of this paper. This work benefited from the use of a large amount of free software, most importantly the MESA stellar-evolution code, IPYTHON/JUPYTER notebooks, PYTHON libraries MATPLOTLIB and PYSHTOOLS, the FFMPEG software suite, Subversion revision control system, or the LaTeX document preparation system.

REFERENCES

Arcavi I. et al., 2017, Nature, 551, 210
Arnett D., 1994, ApJ, 427, 932
Arnett W. D., Meakin C., 2011, ApJ, 733, 78
Bazan G., Arnett D., 1994, ApJ, 433, L41
Bazan G., Arnett D., 1998, ApJ, 496, 316
Biermann L., 1932, Z. Astrophys., 5, 117
Caughlan G. R., Fowler W. A., 1988, At. Data Nucl. Data Tables, 40, 283
Clarkson O., Herwig F., Pignatari M., 2018, MNRAS, 474, L37
Colella P., Woodward P. R., 1984, J. Comput. Phys., 54, 174
Couch S. M., Ott C. D., 2013, ApJ, 778, L7
Couch S. M., Ott C. D., 2015, ApJ, 799, 5
Davis A., Jones S., Herwig F., 2018, MNRAS, 484, 3921
Dayras R., Switkowski Z. E., Woosley S. E., 1977, Nucl. Phys. A, 279, 70
Gilet C., Almgren A. S., Bell J. B., Nonaka A., Woosley S. E., Zingale M., 2013, ApJ, 773, 137
Herwig F., et al., 2018, ApJS, 236, 16
Herwig F., Woodward P. R., Lin P.-H., Knox M., Fryer C., 2014, ApJ, 792, L3
Joggerst C. C. et al., 2014, J. Comput. Phys., 275, 154
Jones S., Andrassy R., Sandalski S., Davis A., Woodward P., Herwig F., 2017, MNRAS, 465, 2991
Kippenhahn R., Weigert A., Weiss A., 2012, Stellar Structure and Evolution. Springer, Berlin
Meakin C. A., Arnett D., 2006, ApJ, 637, L53
Meakin C. A., Arnett D., 2007a, ApJ, 665, 690
Meakin C. A., Arnett W. D., 2007b, ApJ, 667, 448
Mocák M., Meakin C., Campbell S. W., Arnett W. D., 2018, MNRAS, 481, 2918
Müller B., Janka H.-T., 2015, MNRAS, 448, 2141
Müller B., Melson T., Heger A., Janka H.-T., 2017, MNRAS, 472, 491
Ofek E. O. et al., 2014, ApJ, 789, 104
Paxton B., Bildsten L., Dotter A., Herwig F., Lesaffre P., Timmes F., 2011, ApJS, 192, 3
Paxton B. et al., 2013, ApJS, 208, 4
Paxton B. et al., 2015, ApJS, 220, 15
Pignatari M. et al., 2013, ApJ, 762, 31
Pignatari M. et al., 2016, ApJS, 225, 24
Porter D. H., Woodward P. R., 1994, ApJS, 93, 309
Porter D. H., Woodward P. R., 2000, ApJS, 127, 159
Porter D. H., Woodward P. R., Jacobs M. L., 2000, in Buchler J. R., Kandrup H., eds, Annals of the New York Academy of Sciences, Vol. 898, Astrophysical Turbulence and Convection. New York Academy of Sciences, New York, p. 1
Ramaprabhu P., Dimonte G., Woodward P. R., Fryer C., Rockefeller G., Muthuraman K., Lin P. H., Jayaraj J., 2012, Phys. Fluids, 24, 074107
Rauscher T., Heger A., Hoffman R. D., Woosley S. E., 2002, ApJ, 576, 323
Ritter C., Andrassy R., Côté B., Herwig F., Woodward P. R., Pignatari M., Jones S., 2018a, MNRAS, 474, L1
Ritter C., Herwig F., Jones S., Pignatari M., Fryer C., Hirschi R., 2018b, MNRAS, 480, 538
Smith N., Arnett W. D., 2014, ApJ, 785, 82
Smith N., Li W., Filippenko A. V., Chornock R., 2011a, MNRAS, 412, 1522
Smith N., Li W., Silverman J. M., Ganeshalingam M., Filippenko A. V., 2011b, MNRAS, 415, 773
Sytine I. V., Porter D. H., Woodward P. R., Hodson S. W., Winkler K.-H., 2000, J. Comput. Phys., 158, 225
Tur C., Heger A., Austin S. M., 2007, ApJ, 671, 821
Woodward P. R., 1986, NATO Advanced Research Workshop on Astrophysical Radiation Hydrodynamics. in Winkler K.-H. A., Norman M. L., eds, NATO Advanced Science Institutes (ASI) Series C, Vol. 188. D. Reidel Publishing Co., Dordrecht, Holland, p. 245
Woodward P. R., 2007, in Grinstein F. F., Margolin L. G., Rider W. J., eds, Implicit Large Eddy Simulation, Computing Turbulent Fluid Dynamics. Cambridge Univ. Press, Cambridge, p. 130
Woodward P. R., Colella P., 1981, in Reynolds W. C., MacCormack R. W., eds, Lecture Notes in Physics. Springer-Verlag, Berlin, p. 434
Woodward P. R., Colella P., 1984, J. Comput. Phys., 54, 115
Woodward P. R., et al., 2012, in Proc. NECDC2012, Nuclear Explosive Code Development Conference. Livermore, CA, Oct. 2012. Available as Los Alamos National Laboratory internal report LA-UR-13-20949 at http://permalink.lanl.gov/object/tr?what = info:lanl-repo/lareport/LA-UR-13-20949 or at www.lcse.umn.edu/NECDC2012
Woodward P. R., Herwig F., Lin P.-H., 2015, ApJ, 798, 49
Woodward P. R., Herwig F., Wetherbee T., 2018, Comput. Sci. Eng., 20, 8
Woosley S. E., Heger A., Weaver T. A., 2002, Rev. Mod. Phys., 74, 1015

[9] https://zenodo.org/record/2592134
[10] https://goo.gl/8B7w29
[11] https://astrohub.uvic.ca, Herwig et al. (2018)

APPENDIX A: LUMINOSITY CURVES

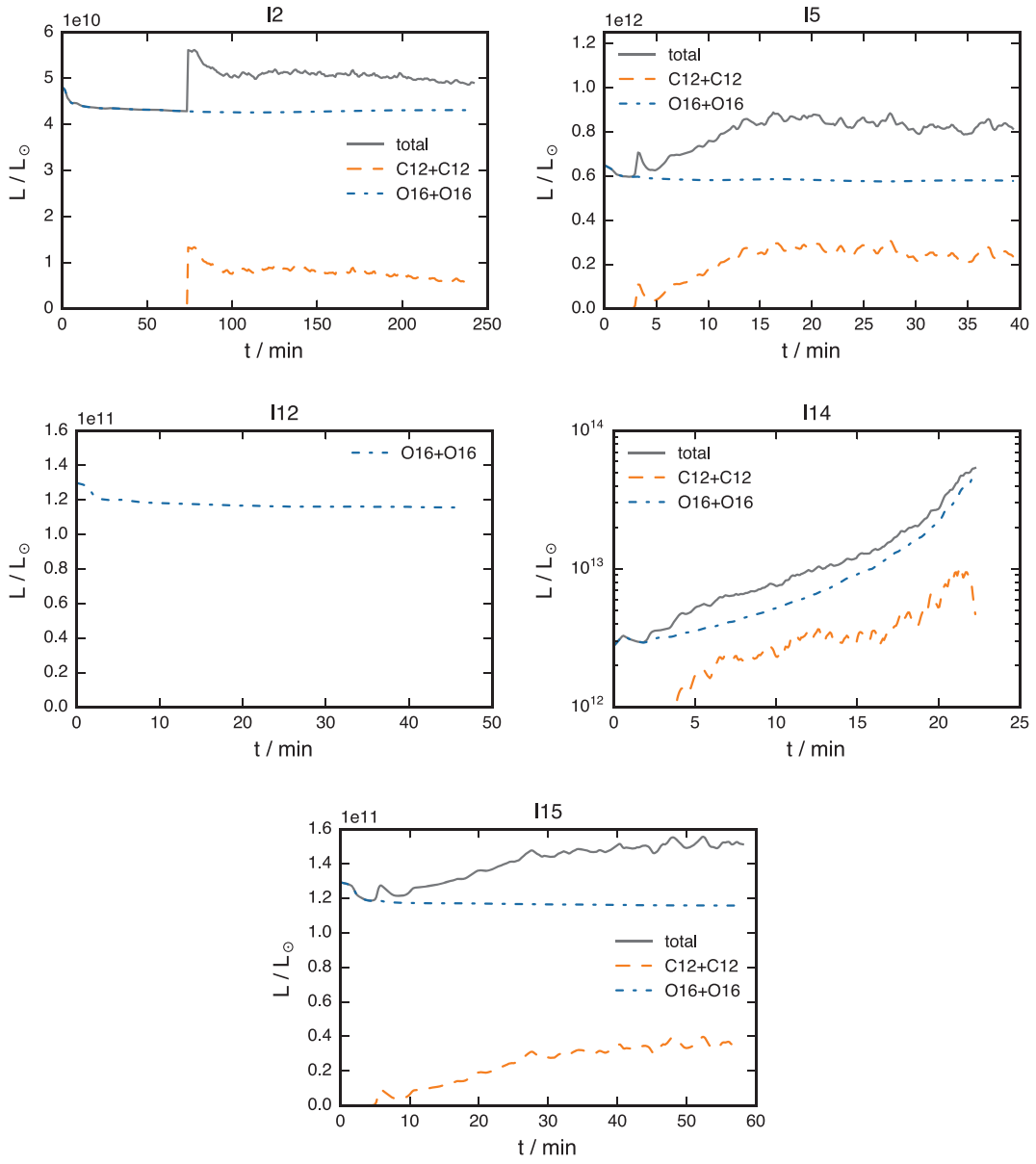

Figure A1. As Fig. 7, but runs I2 ($f_{OO} = 1$, NET 1), I5 ($f_{OO} = 13.5$, NET 1), I12 ($f_{OO} = 2.7$, no C burning), I14 ($f_{OO} = 67.5$, NET 1), and I15 ($f_{OO} = 2.7$, NET 1) are shown.

APPENDIX B: ENTRAINMENT RATE MEASUREMENTS

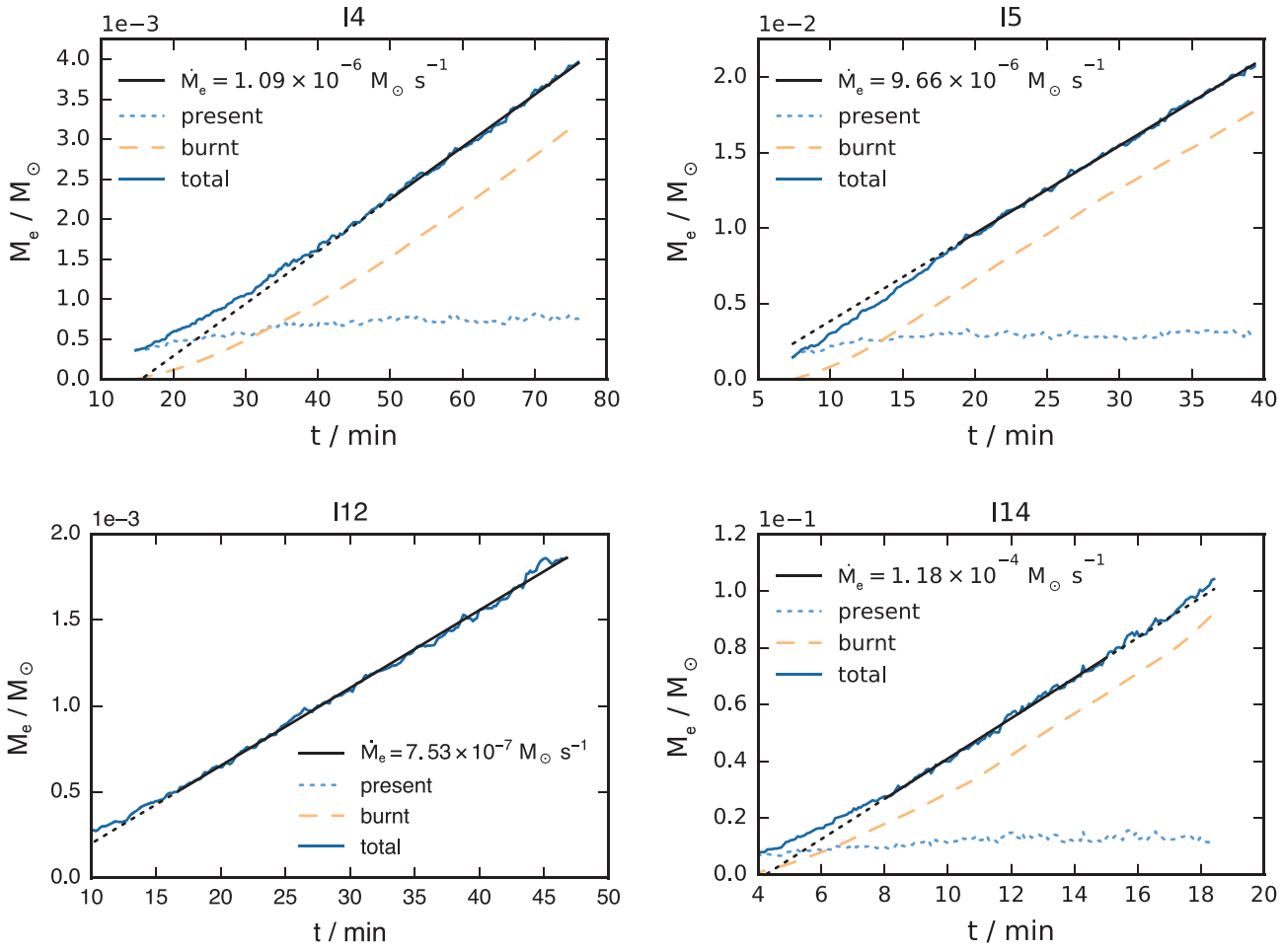

Figure B1. As Fig. 5, but runs I4 ($f_{OO} = 2.7$, NET 1), I5 ($f_{OO} = 13.5$, NET 1), I12 ($f_{OO} = 2.7$, no C burning), and I14 ($f_{OO} = 67.5$, NET 1) are shown.

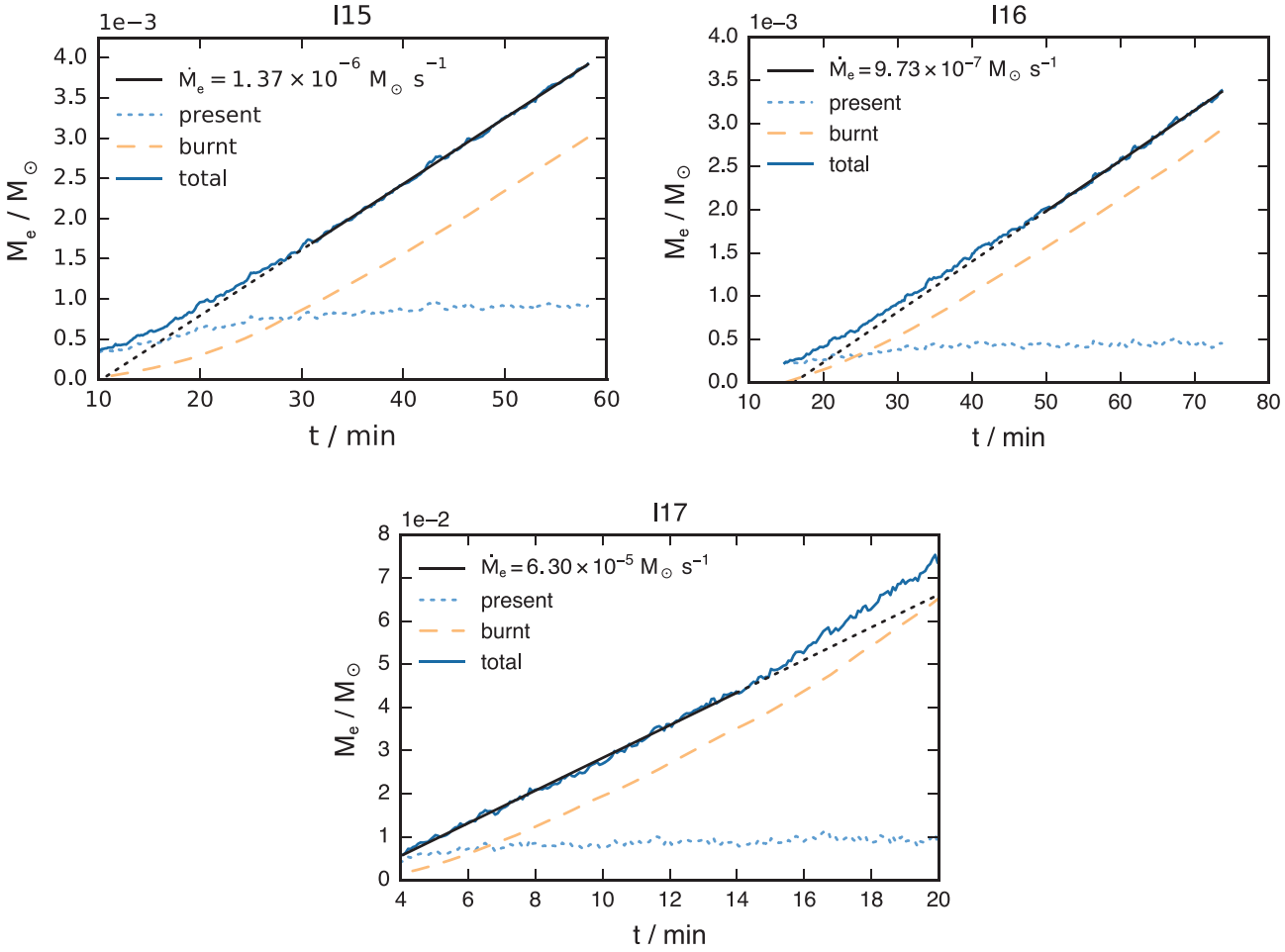

Figure B2. As Fig. 5, but runs I15 ($f_{OO} = 2.7$, NET 1), I16 ($f_{OO} = 2.7$, NET 2), and I17 ($f_{OO} = 67.5$, NET 2) are shown.

APPENDIX C: VELOCITY POWER SPECTRA

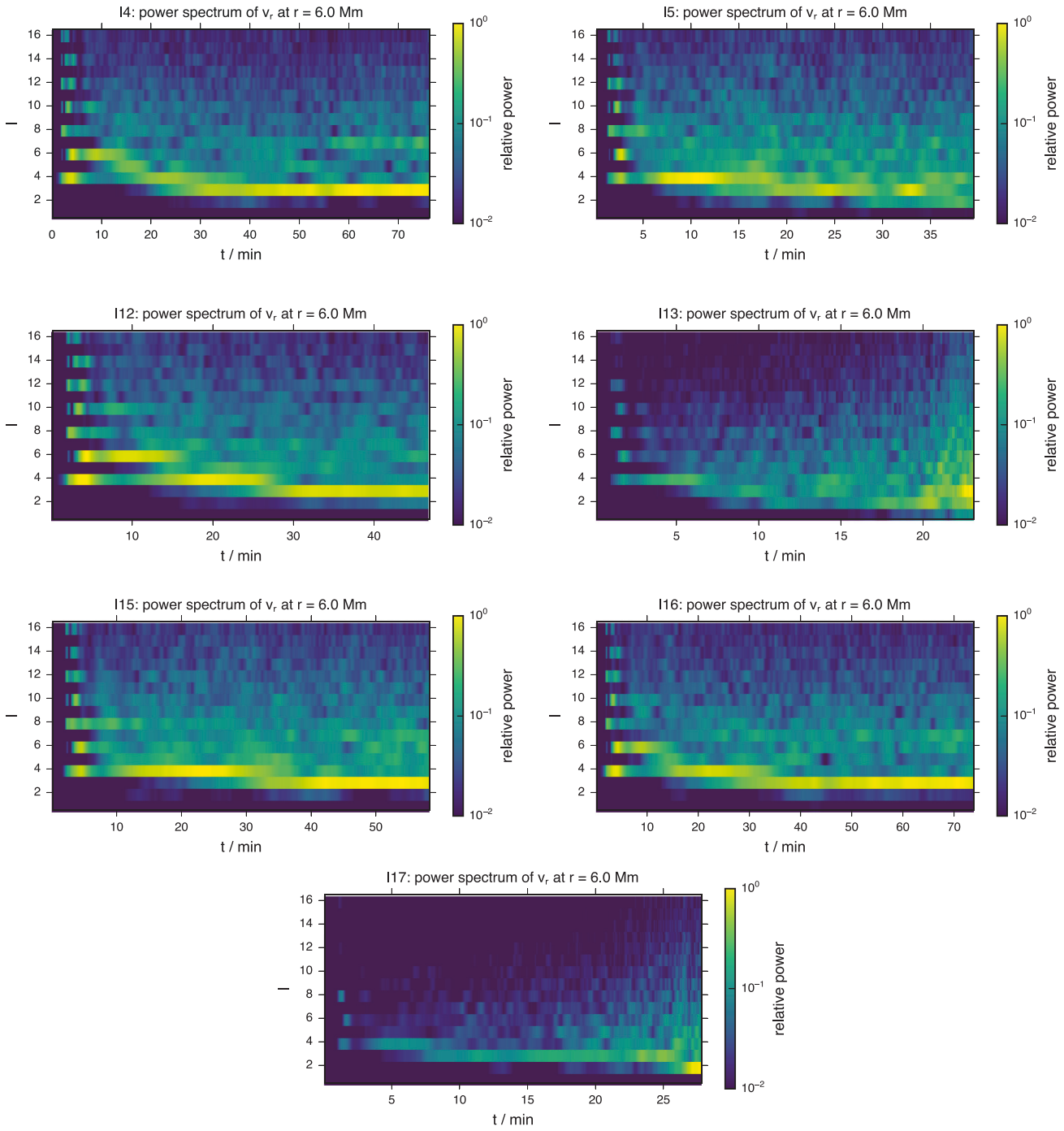

Figure C1. As Fig. 9, but runs I4 ($f_{OO} = 2.7$, NET 1), I5 ($f_{OO} = 13.5$, NET 1), I12 ($f_{OO} = 2.7$, no C burning), I13 ($f_{OO} = 67.5$, NET 1), I15 ($f_{OO} = 2.7$, NET 1), I16 ($f_{OO} = 2.7$, NET 2), and I17 ($f_{OO} = 67.5$, NET 2) are shown.

This paper has been typeset from a TEX/LATEX file prepared by the author.